doi:10.26443/seismica.v4i2.1174

The extremely shallow M_W 4.9 2019 Le Teil earthquake, France: Main ground motion features and comparison with ground motion models

A. Laurendeau *[1], **M. Causse** [2], **E. M. Cushing** [1], **C. Gélis** [1], **M. Lancieri** [1], **R. Rusch** †[1], **P. Fahed**[2], **C. Cornou** [2], **S. Hok** [1]

[1]Autorité de Radioprotection et de Sureté Nucléaire (ASNR), PSE-ENV/SCAN/BERSSIN, F-92260, Fontenay aux Roses, France, [2]University of Grenoble Alpes, University of Savoie Mont Blanc, CNRS, IRD, Univ. Gustave Eiffel, ISTerre, 38000 Grenoble, France

Author contributions: *Conceptualization*: All. *Project Administration*: ML, AL, MC, CC. *Funding acquisition*: ML, CC. *Data Curation*: AL, MC, EMC, CG, ML, RR, PF. *Formal Analysis*: AL, MC, EMC, CG, ML, RR, PF. *Validation*: AL, MC. *Visualization*: AL, MC, EMC. *Writing – original draft*: AL, MC, EMC, ML.

Abstract On 11 November 2019, a M_W 4.9 earthquake occurred in Le Teil, southeastern France, at an exceptional depth of 1 to 2 km. We benefit from a comprehensive dataset of high-quality seismic records to investigate ground motion features in terms of source, path, and site effects. Clear regional variations of intensity measures are identified. Additionally, we conduct a residual analysis by comparing observed motions with predictions from ground motion models (GMMs), revealing a systematic underestimation of amplitudes at low frequencies (< 1 Hz), associated with the generation of Rayleigh waves. These waves are generated due to the shallow depth of the rupture and are most prominent in directions orthogonal to the fault. At higher frequencies, additional spatial variations are observed. In particular, ground motions recorded in the southeast show significantly lower amplitudes than those predicted by GMMs. This phenomenon may be attributed to the regional attenuation and geological structure or to local geological conditions combined with the extremely shallow depth of the seismic event, as demonstrated with numerical simulations. Our study emphasises the necessity for further analyses of ground motions generated by such moderate extremely shallow earthquakes.

Production Editor:
Gareth Funning
Handling Editor:
Pablo Heresi
Copy & Layout Editor:
Miguel Neves

Signed reviewer(s):
Fabian Bonilla

Received:
23 January 2024
Accepted:
11 September 2025
Published:
22 October 2025

Résumé Le 11 novembre 2019, un séisme de M_W 4,9 s'est produit au Teil, dans le sud-est de la France, à une profondeur exceptionnellement faible de 1 à 2 km. A partir d'un large jeu de données sismologiques de haute qualité, nous analysons les caractéristiques du mouvement du sol en lien avec la source, la propagation des ondes et les effets de site. Des variations régionales des mesures d'intensité ont été observées. Une analyse des résidus, comparant les observations aux prédictions de modèles de mouvement du sol (GMM), révèle une sous-estimation systématique des amplitudes aux basses fréquences (< 1 Hz), en lien avec la génération d'ondes de Rayleigh, favorisée par la faible profondeur de la rupture, principalement dans les directions orthogonales à la faille. A plus haute fréquence, d'autres différences spatiales sont observées. En particulier dans la région sud-est, les mouvements du sol présentent des amplitudes largement inférieures aux prédictions. Ce phénomène pourrait être attribué à l'atténuation régionale et à la structure géologique ou aux conditions géologiques locales combinées à la profondeur extrêmement faible de l'événement sismique, comme démontré par des simulations numériques. Cette étude souligne l'intérêt d'approfondir l'analyse des mouvements du sol générés par des séismes modérés extrêmement superficiels.

Non-technical summary On 11 November 2019, a magnitude 4.9 earthquake occurred in Le Teil, Southeastern France, at an unusually shallow depth of 1-2 km, in contrast to most earthquakes that typically originate deeper, beyond 10 km. Recorded by numerous seismic sensors around the epicentre, this event provides a unique opportunity for in-depth analysis of the resulting ground motions, revealing distinct characteristics. Comparison of these observations with statistical models developed from ground motions of other earthquakes, particularly the deeper ones, and used in recent seismic hazard studies, highlights systematic discrepancies. These differences vary depending on the sensor position relative to the earthquake location. We further discuss these variations in light of specific characteristics of this earthquake and the properties of the geological media through which waves propagate. This seismic event challenges conventional expectations and highlights the complexity of shallow earthquakes.

*Corresponding author: aurore.laurendeau@asnr.fr
†Now at Bureau de Recherches Géologiques et Minières (BRGM), DGR/GBS, Orléans, France

1 Introduction

On 11 November 2019, a moderate moment magnitude (M_W) 4.9 earthquake struck the town of Le Teil in southeastern France. This event, hereafter referred to as the Le Teil earthquake, caused a maximum macroseismic intensity of VIII on the EMS-98 scale in certain districts of the town (Cornou et al., 2021; Schlupp et al., 2021). Mainland France is characterised by low-to-moderate seismic activity; the strongest known historical earthquake occurred in 1909, 110 km south of Le Teil, reaching a maximum macroseismic intensity (Imax) of IX on the MSK (Medvedev, Sponheuer and Karnik) scale. Some noteworthy recent seismic events took place in the Pyrenees in 1967 (Arette Imax VIII) and 1980 (Arudy Imax VII), as well as in the Alps in 1996 (Epagny Imax VII) and 2014 (Barcelonnette Imax VI) (Jomard et al., 2021; Scotti et al., 2004). In the vicinity of the Le Teil earthquake, testimonies of some individual historical earthquakes (potentially shallow) with M_W ranging from 3.0 to 4.1 and extremely shallow recent seismic swarms have been documented and observed (Bollinger et al., 2010; Thouvenot et al., 2009; Bollinger et al., 2021; Larroque et al., 2021).

Despite its moderate M_W of 4.9, this reverse-faulting earthquake is associated with up to 15 cm of uplift along the La Rouvière segment of the Cevennes fault system (Ritz et al., 2020). Its hypocentre is extremely shallow, with an estimated depth between 1 and 2 km (Delouis et al., 2021; Vallage et al., 2021). Such shallow nucleation may have been promoted by rock extraction in a nearby quarry (Ampuero et al., 2019, 2020; De Novellis et al., 2020) or meteoric water recharge (Burnol et al., 2023). While this type of earthquake is relatively uncommon worldwide, some moderate M_W extremely shallow earthquakes have been reported notably in China (e.g., Qian et al., 2019; Di et al., 2023), Australia (e.g., Allen et al., 2006; Miller et al., 2023) and northeastern South America (e.g., Barros et al., 2015; Assumpção et al., 2025), sometimes causing locally severe damage. The high level of damage (Imax of VIII) from the Le Teil earthquake and the absence of near fault seismic records motivated a study on ground motion modelling. Based on numerical simulations calibrated with in-situ observations of displaced objects, Causse et al. (2021) demonstrated that vertical ground acceleration locally exceeded gravity. At greater distances from the rupture, macroseismic surveys highlighted a rapid decay of the macroseismic field with distance, faster than for deeper earthquakes (Figure 15 of Schlupp et al., 2021). Numerous papers have been published on the Le Teil earthquake, and only the study by Vallage et al. (2021) has analysed the attenuation of peak ground acceleration (PGA) with distance on a regional scale (307 stations, 850 records), comparing the results with predictive ground motion models (GMMs). They found that observations are mostly lower than predictions for distances less than 100 km.

To date, a comprehensive understanding of the ground motion characteristics of the Le Teil earthquake at a regional scale is lacking. Benefiting from the extensive number of far-field records, our work has three main objectives. Our first objective is to investigate if the ground motions from this moderate extremely shallow event exhibit any potential specific features across different frequencies. Our second objective is to verify if the GMMs used in recent seismic hazard studies are consistent with the ground motions observed during the Le Teil earthquake. Indeed, these GMMs are developed from databases that do not contain earthquakes similar to the Le Teil earthquake (Ancheta et al., 2014; Lanzano et al., 2019b), and may not necessarily reflect the wave propagation characteristics for an extremely shallow moderate event in France. Our third objective is to explore potential explanations for the observed ground motion characteristics in terms of source, path, and site effects.

The paper is organized in four sections. The first section, 2."Data Selection and Processing", describes the ground motion dataset, composed of 198 three-component records at distances ranging from 8 to 300 km. In the second section, 3."Analysis of Main Ground Motion Features", we present the main features of the Le Teil earthquake ground motions (acceleration and velocity peaks, as well as duration), in particular the presence of strong low-frequency waves interpreted as Rayleigh waves. In the third section, 4."Comparison of Observations with GMMs", we correct the observed ground motions for path effects using several GMMs and carry out a residual analysis. We highlight that recorded ground motions of the Le Teil earthquake are generally larger at low frequencies and lower at high frequencies, with a strong azimuthal variability. This variability is further investigated using a clustering approach, which reveals clear spatial patterns. Finally, in the section 5."Interpretation and Discussion", we explore some avenues for the physical interpretation of the observed azimuthal and frequency-dependent variations. It focuses on two main aspects: (1) the systematic underestimation of low-frequency ground motions, which is linked to the generation of Rayleigh waves, and (2) the spatial variations of high-frequency ground motions, attributed to propagation effects, as supported by regional geology and simple 1D numerical simulations. Our study suggests that a better understanding of the ground motions generated by such moderate extremely shallow earthquakes is important to improve seismic hazard assessment.

2 Data Selection and Processing

In recent years, substantial efforts have been dedicated to deploying seismological networks across mainland France. Thanks to these efforts, numerous records of the Le Teil earthquake are available within a 300 km radius around the epicentre (Figure 1). The three-component records are collected from broadband and accelerometric stations distributed through the International Federation of Digital Seismograph Networks (FDSN) Web Services by the European Integrated Data Archive (EIDA) portal (http://www.orfeus-eu.org/data/eida/). Among these, we use 90 stations from the permanent broadband network (Epos-France-RLBP – FR) and 50 from the permanent accelerometric network (Epos-

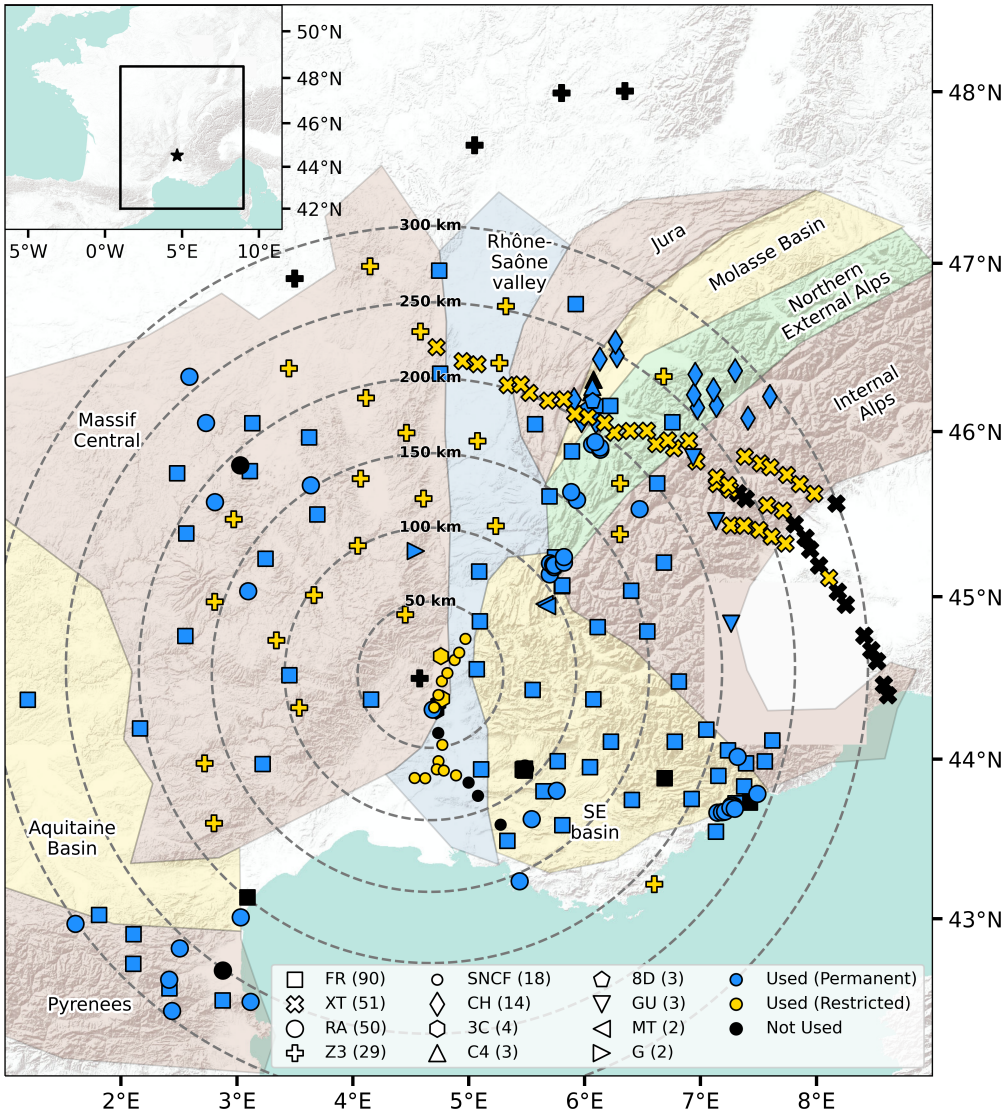

Figure 1 Spatial distribution of the 269 recording stations around the Le Teil earthquake epicentre, part of different networks differentiated by their FDSN codes (see Data and Code Availability - Table 2). The top inset shows a larger view of the study area, with the black rectangle corresponding to the area in the main figure. The earthquake epicentre is represented by a black star in the top inset and is in the main figure at the centre of the circles indicating the epicentral distances between the earthquake and stations. The marker colours distinguish the stations selected in this study from the others in black, with stations from permanent networks available on EIDA in blue and temporary stations from different projects with restricted data or permanent stations with data not normally shared in yellow. A simplified view of the major geological domains around the earthquake is also superimposed on the map using coloured polygons, with the Rhône-Saône River valley in blue, the sedimentary basins in yellow, the crystalline mountains in brown and the deformed northern external domain of the Alps in green.

France-RAP – RA). The closest FR and RA stations to the rupture are OGDF (30 km) and OGLP (22 km), respectively (Figure 1. stations with codes FR and RA in blue).

Within the epicentral area, we also include data from restricted-access or dedicated networks not typically available through public archives (Figure 1. stations in yellow):

- Three temporary broadband stations were installed in the Tricastin nuclear power plant area as part of a scientific project led by the *"Institut de Radioprotection et Sûreté Nucléaire"* [IRSN], focusing on seismic site effect estimation (Froment et al., 2022; Gélis et al., 2022), and one accelerometric station operated by the French nuclear operator *"Electricité De France"* [EDF] is located near the Cruas nuclear power plant (~12 km from the rupture), totalling 4 stations (code 3C).

- The "*Société Nationale des Chemins de fer Français*" [SNCF] provides records from 18 triggered accelerometric stations deployed along the Mediterranean high-speed railway line [LGV], as part of an earthquake emergency stopping system operated by the French Alternative Energies and Atomic Energy Commission [CEA] (Vallage et al., 2021, code SNCF). Nine of the SNCF stations are within 50 km of the epicentre, with the closest one located 8 km

from the rupture.

To enrich the far-field dataset, we incorporate temporary broadband stations from two major scientific projects (Figure 1. stations in yellow):

- The CIFALPS-2 project (Zhao et al., 2018) provides data from 51 stations spaced 5–10 km apart across the northwestern Alps and Ligurian Alps, located at least 200 km from the La Rouvière fault (code XT).
- The AlpArray project (Hetényi et al., 2018) contributes 29 stations spaced ∼52 km across the Alpine regions, enhancing data coverage west and north of the epicentre. The nearest usable record from this network is located about 40 km from the rupture (code Z3).

The overall characteristics of the networks are summarized in the "Data and Code Availability" section (Table 2). As a result, we compile an initial dataset of 269 three-component records from accelerometric and broadband stations (Figure 1).

All records undergo visual inspection to remove defective waveforms (e.g., clipped waveforms, train waves in SNCF data, ...). Then, the frequency band for which seismic energy is available for analysis is defined following the PEER procedure (Ancheta et al., 2013) by ensuring that the Fourier spectra of the signal are at least three times greater than those of the noise, and checking that no linear trends remain in the displacement signal. An acausal Butterworth filter is then applied to the acceleration signal within this range. Details on signal processing are provided in the Supplementary Text S1. Finally, only waveforms with a usable frequency band extending beyond 0.5–5 Hz are selected. The usable frequency band is defined as the bandpass filter frequencies scaled inward by a factor of 1.25, as is classically done in GMM flatfiles (e.g., Ancheta et al., 2014; Traversa et al., 2020). In cases where records are available for two co-located sensors (an accelerometer and a broadband sensors), the accelerogram records (HN channels) are preferred. This is because French accelerometers are typically installed at the surface, whereas broadband sensors can be placed at depth in boreholes to enhance the signal-to-noise ratio. However, this configuration can result in a deamplification of the seismic signal at high frequencies (Hollender et al., 2020). The final dataset is composed of 198 three-component stations well-distributed around the Le Teil earthquake epicentre and covering different major geological domains (Figure 1).

3 Analysis of Main Ground Motion Features

In this part, our goal is to identify potential specific features of the Le Teil earthquake ground motions. To achieve this aim, we examine the spatial distribution of some ground motion intensity measures, such as acceleration and velocity peaks, as well as duration. Additionally, we conduct a time-frequency analysis of ground motion at three representative stations.

3.1 Intensity Measure Maps

We estimate the intensity measures using a Seismic-Intensity-Measure code developed in Python, and the values are provided in an Excel table as supplementary material and available on Zenodo (See Data and Code Availability section, Laurendeau et al., 2024). Figure 2 displays the spatial distribution of the geometrical mean of the two horizontal components for three intensity measures: Peak Ground Acceleration (PGA), Peak Ground Velocity (PGV) and significant relative duration ($D_{SR\text{-}5\text{-}95\%}$, see Bommer et al., 2009). The highest recorded PGA is 76 cm/s^2, observed at CAI55 by the SNCF network located 10 km from the rupture fault. As expected, PGA values decrease with increasing distance, although spatial variations are evident based on major geological domains (Figure 1 and Figure 2). At distances of 100–150 km from the La Rouvière fault in the Massif Central, PGAs are around 1 cm/s^2, five times higher than those recorded in the Alps around 0.2 cm/s^2. At distances of 250–300 km, PGAs recorded in the Pyrenees are around 0.1 cm/s^2 and in the Alps around 0.04 cm/s^2. Thus, a faster decay of PGA with distance is observed southeast of the rupture compared to the northwest region. The highest PGV, equal to 3 cm/s, is recorded at P55 by the SNCF network located 8 km from the rupture fault. The spatial distribution of PGV values appears fairly similar to that of PGA values, except for the area to the south-southeast of the rupture, where there are no longer significant differences in PGV values at the same distances compared to the northwest. $D_{SR\text{-}5\text{-}95\%}$ increases with distance, and shorter seismic signals are observed in the northwest compared to the southeast. For example, at distances of 100–150 km from the La Rouvière fault, durations are longer in the southeast by at least 20 seconds. The analysis of the spatial distribution of these intensity measures reveals distinct behaviours between the regions around the epicentre, with a clear separation between the northwest and southeast. The observed differences between PGA and PGV values also suggest variations in the ground motion frequency content.

3.2 Focus on Three Representative Stations

To further investigate the spatial variations highlighted above, we conduct an in-depth analysis of signals from three representative stations: OCOL, OGCH, and IRVG (locations in Figure 2). These stations are selected based on their positions at three different azimuths from the Le Teil rupture (OCOL to the northwest, OGCH to the northeast, and IRVG to the southeast), at similar distances (~120–150 km), and especially because they are on rock sites ($V_{S30} \geq 1400$ m/s), minimizing the impact of soil conditions on the signals. It is noteworthy that all three stations are accelerometers from the RA network, facilitating data comparisons.

Figure 3 illustrates the three-component velocity time series at these stations, as well as their time-frequency representations (Stockwell et al., 1996). For this analysis, the north and east horizontal components are rotated into radial and transverse components. The figure in acceleration is provided in the supplementary mate-

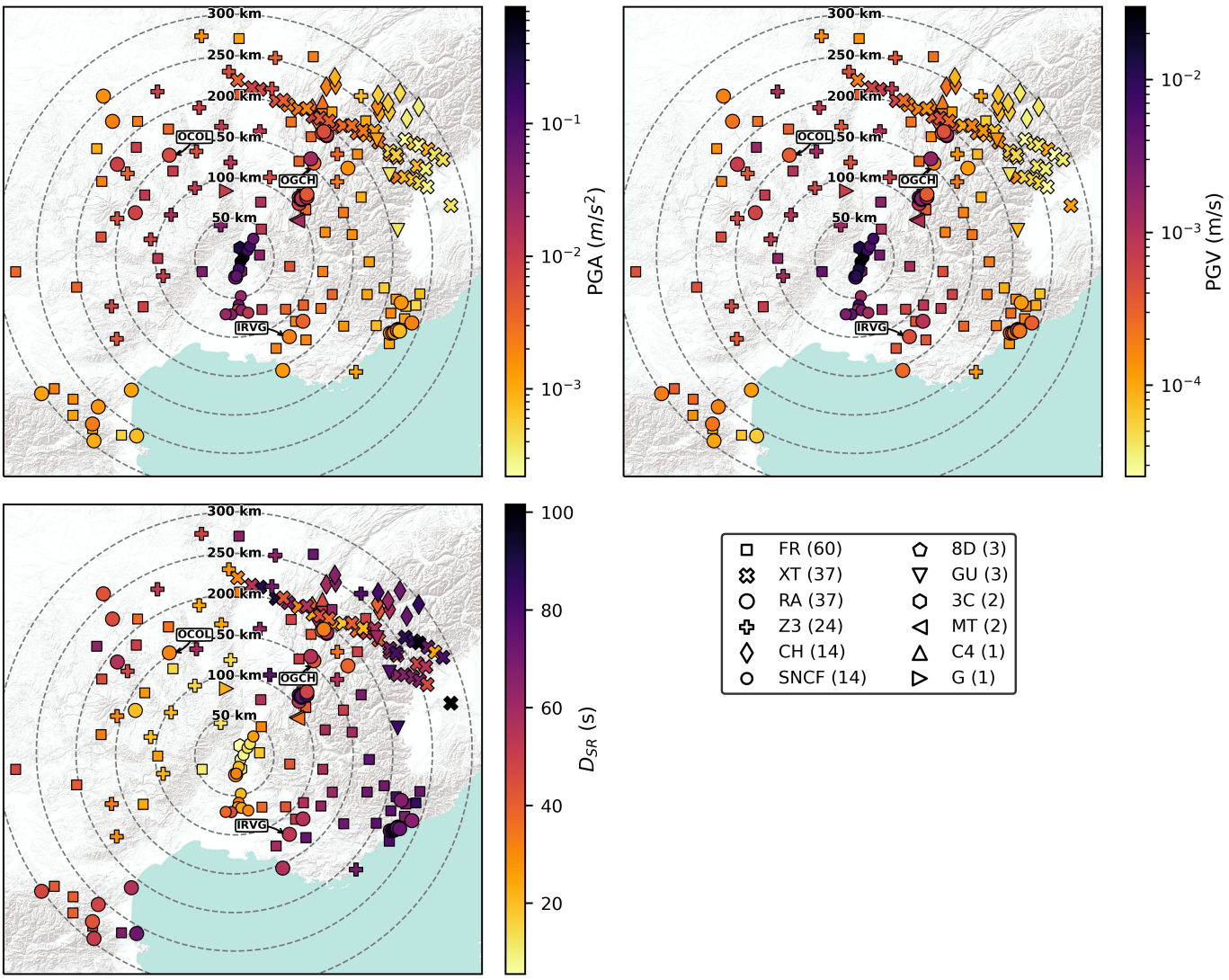

Figure 2 Spatial distribution of three intensity measures (IMs) around the Le Teil earthquake epicentre recorded by the 198 stations: top-left panel, PGA values (m/s^2), top-right panel, PGV values (m/s) and bottom-left panel, $D_{SR\text{-}5\text{-}95\%}$ (s). The three IMs are computed as the geometrical mean of the two horizontal component values. The waveforms of the three stations (OCOL, OGCH, IRVG) indicated in the maps are analysed in Figure 3.

rial (see Figure S.2). Firstly, differences are observed in the acceleration waveforms, with more impulsive signals for OCOL and OGCH, characterised by a large-band increase in energy for body-waves, particularly rich in high frequencies. In contrast, the signal at IRVG is more elongated in time and has a poorer high-frequency content. Additionally, the Stockwell transform at IRVG exhibits less high frequency after 40 seconds, and the high-frequency decay of the Fourier spectrum is faster than for the other two selected stations. This is consistent with previous observations that northwest and northeast stations have stronger PGA and shorter durations compared to southeast stations (see Figure 2 and S.2). Secondly, examining the low-frequency part of the signal, the time-frequency analysis reveals an energy increase at the OCOL and IRVG stations on the radial and vertical components between around 30 and 50 seconds and for frequencies below 1 Hz. These waves are spread out over time, with the lowest frequencies arriving first and then the highest frequencies with energy between 0.4 and 1 Hz. Given this dispersive feature and the presence of these waves in the radial and vertical components, they are interpreted as Rayleigh waves. These waves are less visible on the Stockwell transform at IRVG than at OCOL due to a more complex signal. They are well visible on the waveforms (Figure 3 - grey rectangles), supporting the PGV at IRVG station for the radial and vertical components and at OCOL station for the radial component. At OCOL, the amplitudes of the Fourier spectra of the radial and vertical components are notably greater than the transverse component between 0.1 and 0.5 Hz. This can also be observed at IRVG but not across the entire frequency range of 0.1–0.5 Hz. Conversely, at station OGCH, it is not possible to identify these Rayleigh waves. This observation is also consistent with PGV observations (Figure 2), where no significant difference was noted between the northwest and south-southeast, while lower PGV_S were observed in the northeast.

Thus, the spatial distribution of intensity measures and the waveform analysis at three representative stations highlight (1) a faster decay of high-frequency

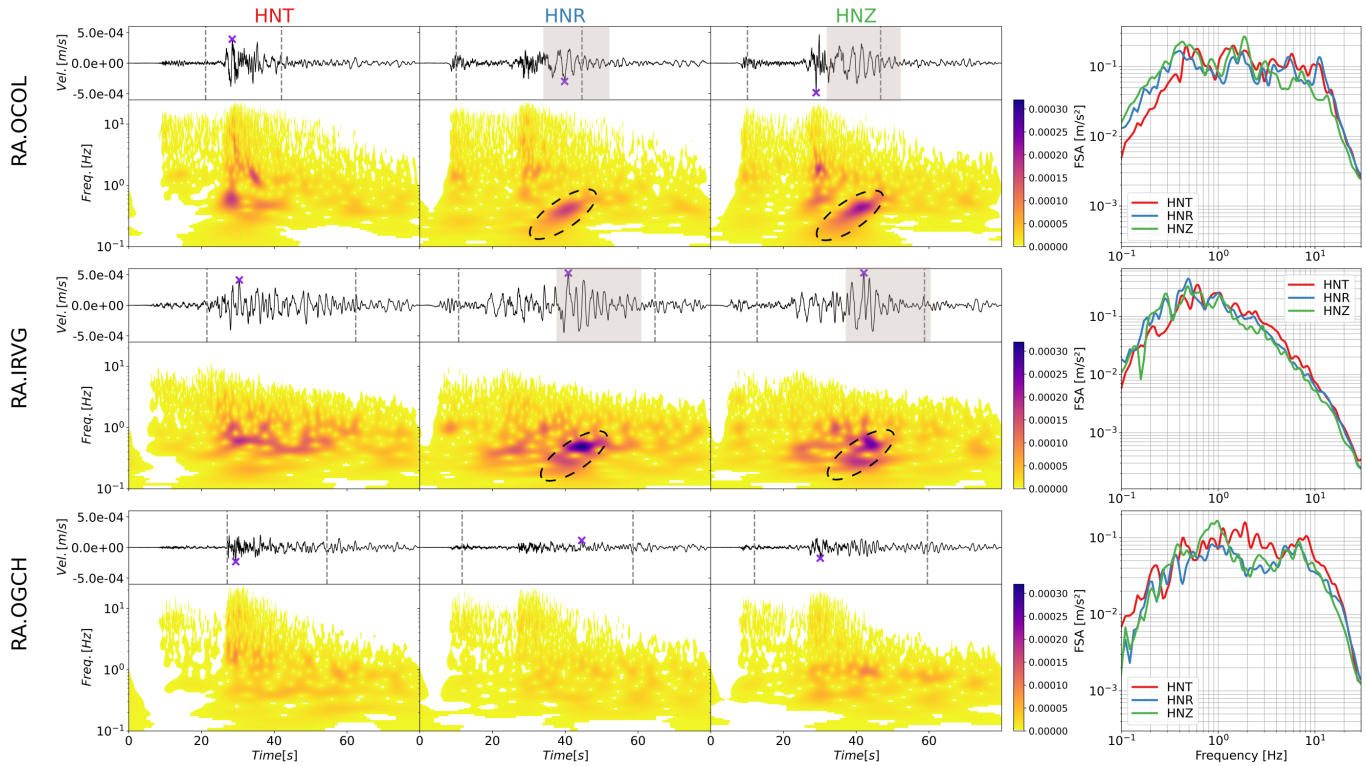

Figure 3 Waveforms in velocity, corresponding Stockwell transform and Fourier spectra in acceleration for the OCOL (northwest), IRVG (southeast) and OGCH (northeast) stations for the transverse (red), radial (blue) and vertical (green) components. The location of the three stations is given in Figure 2. The presence of Rayleigh waves at OCOL and IRVG is indicated by grey rectangles on the waveforms and dotted lines on the Stockwell transforms. On the waveforms, the purple cross indicates the PGV, and grey vertical dotted lines indicate the significant relative duration, i.e., the time interval between 5% and 95% of the cumulative Arias Intensity over time ($D_{SR\text{-}5\text{-}95\%}$). The same figure in acceleration is provided in the supplementary material (see Figure S.2).

ground motion with distance in the southeast direction and (2) the prevalence of Rayleigh waves for frequencies lower than 1 Hz in the northwest-southeast directions. We will propose several physical interpretations to these observed differences in section 5."Interpretation and Discussion", but first, we further investigate the specific features of the Le Teil earthquake through a comparison with GMMs.

4 Comparison of Observations with GMMs

This part aims to achieve two main objectives: (i) to highlight any specific ground motion features by analysing the ground motion residuals (i.e., the difference between observations and GMM predictions), obtained by correcting for path effects using various GMMs, and (ii) to verify the ability of GMMs employed in recent seismic hazard studies to predict the Le Teil earthquake ground motions, knowing that the databases used for their development lack data with identical scenario characteristics. To perform this comparative analysis, five GMMs are selected, comprising three GMMs developed from global databases (Boore et al., 2014; Chiou and Youngs, 2014; Cauzzi et al., 2015) and two from European-Mediterranean databases (Bindi et al., 2014; Kotha et al., 2020, 2022). These models are selected based on their recent use in seismic hazard studies predicting ground motions of shallow crustal earthquakes in active tectonic regions (e.g., Weatherill and Danciu, 2018; Beauval et al., 2020; Weatherill et al., 2020; Türker et al., 2022). Main characteristics of these GMMs are summarized in Table S.1.

For each station, the geometric mean (GM) and the orientation-independent, non-geometric mean (RotD50) (Boore, 2010) are computed from the two horizontal components to maintain consistency with the definitions used in the selected GMMs. This RotD50 value is used only if it is included within the usable frequency band (defined in the part 2."Data Selection and Processing"). The input parameters required for these GMMs, or to compute them, are presented in Table 1. Site-to-fault distances (R_{JB}, R_{RUP}, and R_X) are computed by approximating the fault as a rectangular plane. The location, strike and length of the fault plane on the surface are determined based on the trace of the fault observed from InSAR analysis (Ritz et al., 2020) (approximately 5 km on the InSAR image). The fault width is estimated from the slip inversion results (Vallage et al., 2021; Cornou et al., 2021). Finally, these GMMs employ the V_{S30} parameter, which represents the time-averaged shear wave velocity in the top 30 m of soil and provides a first-order estimate of subsoil stiffness at the surface, particularly in the presence of soft shallow layers, although it does not fully capture site response (e.g., Castellaro et al., 2008; Cadet et al., 2010). In this study,

V_{S30} is available for only 32 of the 198 stations used (see Figure S.3). Most of these values were obtained from characterisation campaigns conducted within the framework of the Epos-France-RAP projects (Regnier et al., 2010; Hollender et al., 2018) and are published in the Epos-France-RAP and -RLBP dataset (Traversa et al., 2020). For the IRSN station named ADHE, as well as for the SNCF station named P71, located in similar geological conditions, the V_{S30} value is provided by Gélis et al. (2022). For stations without measured V_{S30} values, a common approach in GMM development is to estimate V_{S30} from topographic slope (e.g., Wald and Allen, 2007), and such proxies have been widely used in recent studies (e.g., Lanzano et al., 2019a). However, a preliminary comparison with French data shows a poor correlation between slope-based estimates and measured V_{S30} values, particularly for hard-rock sites on low-slope limestone plateaus in southeastern France (see Figure S.4). This observation is consistent with the findings of Lemoine et al. (2012), who advise against the use of slope-based proxies for local studies in such geological contexts. To minimize the bias introduced by unreliable proxy values, we choose to assign a uniform V_{S30} value of 800 m/s to all stations in the main analysis presented in this paper. The impact of this assumption is illustrated in Figure S.5, which shows how ground motion predictions change when using V_{S30} values of 300 m/s or 2000 m/s instead of 800 m/s. Additionally, we provide in the Supplementary Material alternative analyses using other plausible V_{S30} values to assess the robustness of our conclusions. These tests indicate that the various assumptions for the V_{S30} values have no impact on the main conclusions of our study, as explained subsequently.

Table 1 Parameters used in the selected GMMs and for computing various distance definitions between the fault and each recording station.

M_W	4.9
Focal Depth (km)	1
Hypocentre Latitude (°)	44.5178
Hypocentre Longitude (°)	4.6709
Z_{TOR} (km)	0
Strike (°)	45.16
Rake (°)	82
Dip (°)	45
Reference Latitude (°)	44.509
Reference Longitude (°)	6.638
Fault width (km)	2
Fault length (km)	5.09
V_{S30} (m/s)	800

4.1 Spectral Accelerations vs Distance

Figure 4 compares the spectral accelerations observed and predicted by five GMMs (median values) as a function of distance for four frequencies. Firstly, the comparison of the GMMs reveals differences depending on frequency and distance. At low frequencies, all five GMMs predict relatively similar spectral accelerations, except for near-fault distances (< 20 km). This variation can be attributed to the use of different sites-to-fault distance definitions: CY14 and Ca15 use R_{RUP} and predict the highest spectral accelerations, whereas the other GMMs use R_{JB}, and thus are calibrated on the median of ground motions generated by earthquakes of various depths. Among the GMMs using the R_{JB} distance, which does not account for the earthquake's depth, Ko20 predicts the highest spectral acceleration at short distances. This model is unique in that it is defined for three different classes of hypocentral depth, and the class used here corresponds to hypocentral depths lower than 10 km. As the frequency increases, discrepancies between GMMs become more apparent at large distances, reflecting differences in the term describing the attenuation of seismic waves. Ko20 and CY14 exhibit the highest ground motion attenuation at large distances, while Bi14 has the lowest attenuation.

Secondly, when comparing the observed data to the GMM predictions, several trends are observed. At low frequencies (0.5 Hz and 1 Hz), the observations tend to be higher than the median GMM predictions, with some observations being up to five times higher than the median predicted values at distances up to 150 km. At 2 Hz, observations closely align with the predictions, while at higher frequencies, observations are mostly below predictions, except for the three closest stations. Notably, at large distances (> 100 km), there is a large dispersion in the observations, with the Ko20 and CY14 models appearing to be median for these observations.

4.2 Residual Analysis

To highlight the main features of the Le Teil earthquake and assess the ability of GMMs to predict observations, a residual analysis is conducted. The GMM can be expressed in a general form as follows:

$$\ln\left(SA_{obs}(f)\right)_{es} = f\left(PV, \theta(f)\right) + \epsilon(f)_{es} \quad (1)$$

where $SA_{obs}(f)$ represents the observed response spectrum for an earthquake *e* at a station *s*, *f(PV,* θ*)* is the median ground motion model with *PV* as the vector of predictor variables (e.g. earthquake magnitude, distance to ruptured area, etc.) and θ the vector of model coefficients, and $\epsilon(f)_{es}$ is the total residuals, called hereafter epsilon. $\epsilon(f)_{es}$ represents the log-difference between observed spectral acceleration (SA_{obs}) and median predictions (SA_{pred}). This term can be decomposed into repeatable and aleatory components using mixed-effects regression methods (Abrahamson and Youngs, 1992; Al Atik et al., 2010):

$$\epsilon(f)_{es} = \delta B_e(f) + \delta W_{es}(f) \quad (2)$$

where δB_e and δW_{es} are the between-event and within-event components of residuals, respectively. δB_e represents the average shift of all ground motions recorded for an earthquake from the median ground motion calculated using a GMM. It is generally interpreted as a term quantifying remaining source effects averaged over all azimuths. It reflects the influence of factors such as stress drop (e.g., Bindi et al., 2017; Oth et al., 2017) and slip variation in space and time that are

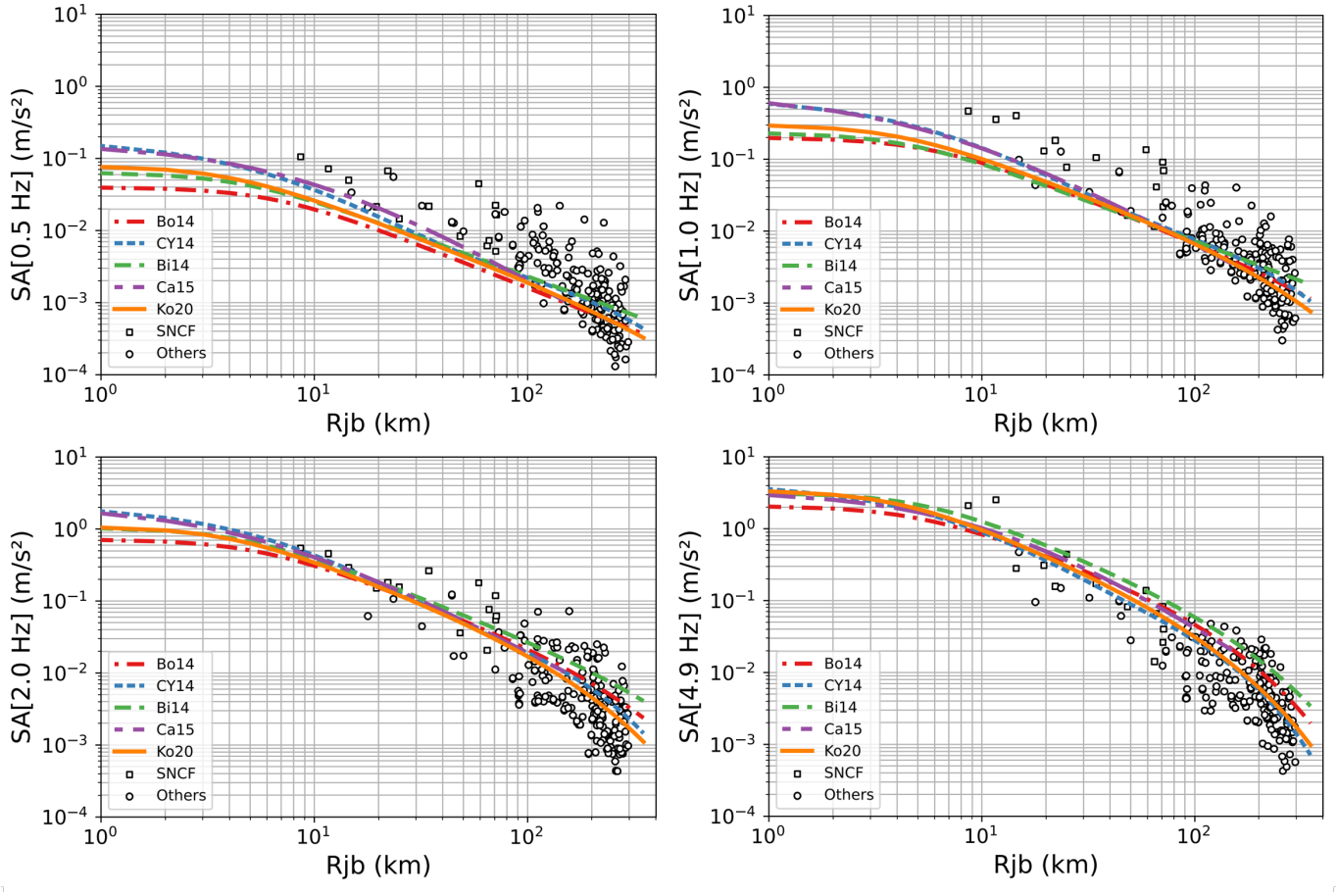

Figure 4 Spectral acceleration (SA) in m/s^2 for five ground motion models compared to observations of the Le Teil earthquake defined in RotD50 for four different frequencies in terms of R_{JB} distance definition. To facilitate model comparison across various distance definitions, we adopt the assumptions $R_{JB} = R_{RUP}$ and R_X=- R_{JB}. The V_{S30} parameter is set to 800 m/s in the GMMs.

not modelled by the source predictor variables of the model, such as the magnitude and the source depth. δB_e can be computed using the formulation of Abrahamson and Youngs (1992):

$$\delta B_e(f) = \frac{\tau(f)^2 \sum_{s=1}^{n_e} SA_{obs_{es}}(f) - SA_{pred_{es}}(f)}{n_e(f)\tau(f)^2 + \varphi(f)^2} \quad (3)$$

where n_e is the number of observations for the considered earthquake, τ and φ are the standard deviations of the between-event and within-event components, respectively, defined for the selected GMM. δW_{es} represents the remaining differences in source, path, and site effects not captured by distance and site variables, once δB_e has been considered.

4.2.1 Between-Event Residuals

Figure 5 displays δB_e computed from the five selected GMMs and for the Le Teil earthquake ground motions. Figure 6 illustrates these residuals for the three representative stations already presented in section 3."Analysis of Main Ground Motion Features". As a reminder, the main analysis presented here assumes a fixed V_{S30} value of 800 m/s for all stations, as justified before. δBe values for all GMMs are positive at low frequencies (< 1 Hz), reaching values up to unity, suggesting that, on average, all GMMs underestimate the low-frequency ground motions of the Le Teil earthquake (Figure 5). Figure 6 (left panels) highlights a bump in the observed acceleration response spectra for stations OCOL and IRVG, not predicted by the Ko20 GMM, resulting in positive epsilon values (in blue). The δB_e-corrected prediction (in green) better matches the observed spectra at low frequencies for stations OCOL and IRVG. The positive δB_e in Figure 5 probably reflects the presence of a dominant number of stations with this special feature. At high frequencies (> 1 Hz), δB_e values computed with different GMMs exhibit wide variability (Figure 5), with slightly positive values for CY14 and negative values around -1.5 for Ca15, indicating a substantial overestimation of predictions compared to observations.

4.2.2 Within-Event Residuals

In the following, the Ko20 GMM, on which the 2020 update of the European Seismic Hazard Model (ESHM20 Danciu et al., 2021), is retained for presenting the within-event residuals, δW_{es}. Ko20 has the advantage of being less dependent on the V_{S30} parameter than other GMMs, minimizing the impact of assuming V_{S30} = 800 m/s (see Figure S.5). Furthermore, we verified that δB_e values computed with Ko20 are poorly sensi-

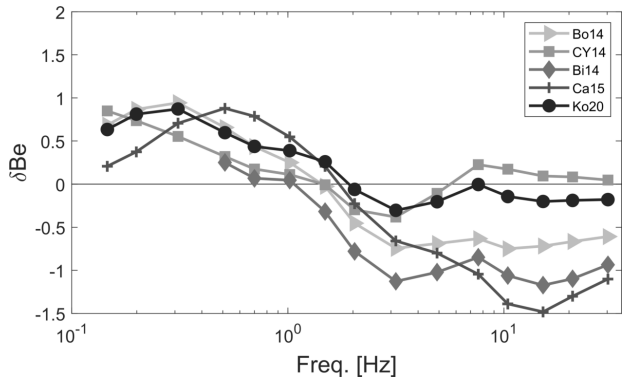

Figure 5 Between-event residuals (δB_e) computed from the five GMMs with respect to the frequency. Note that for each frequency, the number of stations used to compute δB_e varies according to the usable frequencies for each record, and for Ca15, δB_e is computed using a reduced number of stations compared to other GMMs, as this model is defined for R_{RUP} up to 150 km (Table S.1).

tive to the selected V_{S30} values (either the default 800 m/s or measured values or inferred from the topographic slope) and to the considered distance range (see Figure S.6). Once δB_e is defined from Ko20 under the assumption of V_{S30} = 800 m/s, δW_{es} is calculated from (*1*) and (*2*).

Firstly, it is insightful to examine these within-event residuals for the three representative stations OCOL, IRVG, and OGCH (Figure 6, right panel, green lines). Three distinct behaviours are observed:

1. For the OCOL station (northwest), δW_{es} is close to zero up to 3 Hz and positive for higher frequencies.
2. For the IRVG station (southeast), δW_{es} displays slightly positive values up to 0.7 Hz, followed by a clear downward trend in the high-frequency range, forming an 'S-shape' residual pattern.
3. For the OGCH station (northeast), δW_{es} is negative at low frequency and slightly positive at high frequency.

For these three stations, we also compare results using measured V_{S30} values (> 1400 m/s) instead of the default 800 m/s. While this leads to some differences, mainly at high frequencies, the main spectral features, including the 'S-shape' at IRVG and the low high-frequency content, remain consistent. Thus, OCOL and IRVG behave similarly at low frequencies, while OCOL and OGCH exhibit similar behaviour at high frequencies.

Secondly, the spatial distribution of δW_{es} across all stations defined from Ko20 is analysed at different frequencies (see Figure 7). Results from other GMMs are provided as supplementary material (see Figures S.7 to S.10). Darker shades of red indicate higher observations than δB_e-corrected predictions and darker shades of blue indicate lower observations than δB_e-corrected predictions. White indicates cases where δB_e-corrected predictions match observations. At 0.5 Hz, most stations in the western (e.g., OCOL) and southeastern (e.g., IRVG) regions show δW_{es} close to zero (light colours), while stations in the northeastern part (e.g., OGCH) at long distances (> 100 km) in the Alpine topographies (and also some stations in the eastern Pyrenees) predominantly have negative δW_{es} values (in blue). This negative region extends south-eastward with increasing frequency, resulting in two distinct zones at 5 Hz: predominantly positive δW_{es} values appear northwest of the rupture (e.g., OCOL), and negative values are southeast of the rupture (e.g., IRVG). In the latter case, some stations exhibit particularly negative δW_{es} values (in dark blue), as seen in the case of IRVG.

To assess the robustness of the results, two additional sensitivity analyses are performed. First, we tested the influence of the V_{S30} values on the spatial distribution of δWes by (1) using only the 32 stations with measured V_{S30}, and (2) including all stations, assigning slope-based V_{S30} estimates to those without measurements (see Figures S.11 and S.12). In both cases, the observed patterns remain consistent with those in Figure 7. Second, we test the regional GMM of Kotha et al. (2020), in which the random part $\epsilon(f)_{es}$ is decomposed into several components, in particular by looking in a specific region at the repetitive effects of (1) earthquakes, representative of earthquake locality-to-locality variability δ_{L2L}, and (2) path, representative of the region-specific anelastic attenuation δ_{c3}. By correcting the median spectrum for these two variables, a region-specific prediction is obtained. The model indicates higher attenuation (δ_{c3}) in the southeast at 10 Hz. Nevertheless, the overall within-event residual patterns remain consistent with those obtained using the median Ko20 model, with very low δW_{es} values in the southeast (see Figure S.13).

Finally, to explore if the three δW_{es} patterns identified at the representative stations (OCOL, IRGV, and OGCH, Figure 6) can be extended spatially on a broader scale, we employ the k-means clustering algorithm (Arthur and Vassilvitskii, 2007) to classify all stations into distinct groups with similar δW_{es} characteristics. K-means clustering is a data-driven method that assigns each station to the nearest cluster centroid in a feature space, where proximity is measured using the L2-norm between δW_{es} observations. As such, stations located near cluster boundaries may share characteristics with multiple clusters, and their final assignment can be sensitive to small variations in the input data or initialisation (Jain, 2010). This approach thus provides a simplified categorisation that highlights dominant spatial trends, rather than strict, sharply defined groupings.

We select 182 stations for which response spectra, and thus δW_{es}, are defined between 0.4 and 7 Hz. After several trials and errors, we determine that four clusters effectively capture the main regional features of δW_{es} identified in the previous section. Figure 8 displays the δW_{es} curves of these four clusters and their spatial distribution on a map. Clusters #1 to #3 each include one of the three representative stations OGCH, OCOL and, IRVG, respectively. Overall, stations in the vicinity of these three representative stations are assigned to the same cluster and exhibit similar variations in δW_{es} with frequency. In contrast, cluster #0 (in red) stands out by grouping spatially scattered stations that neverthe-

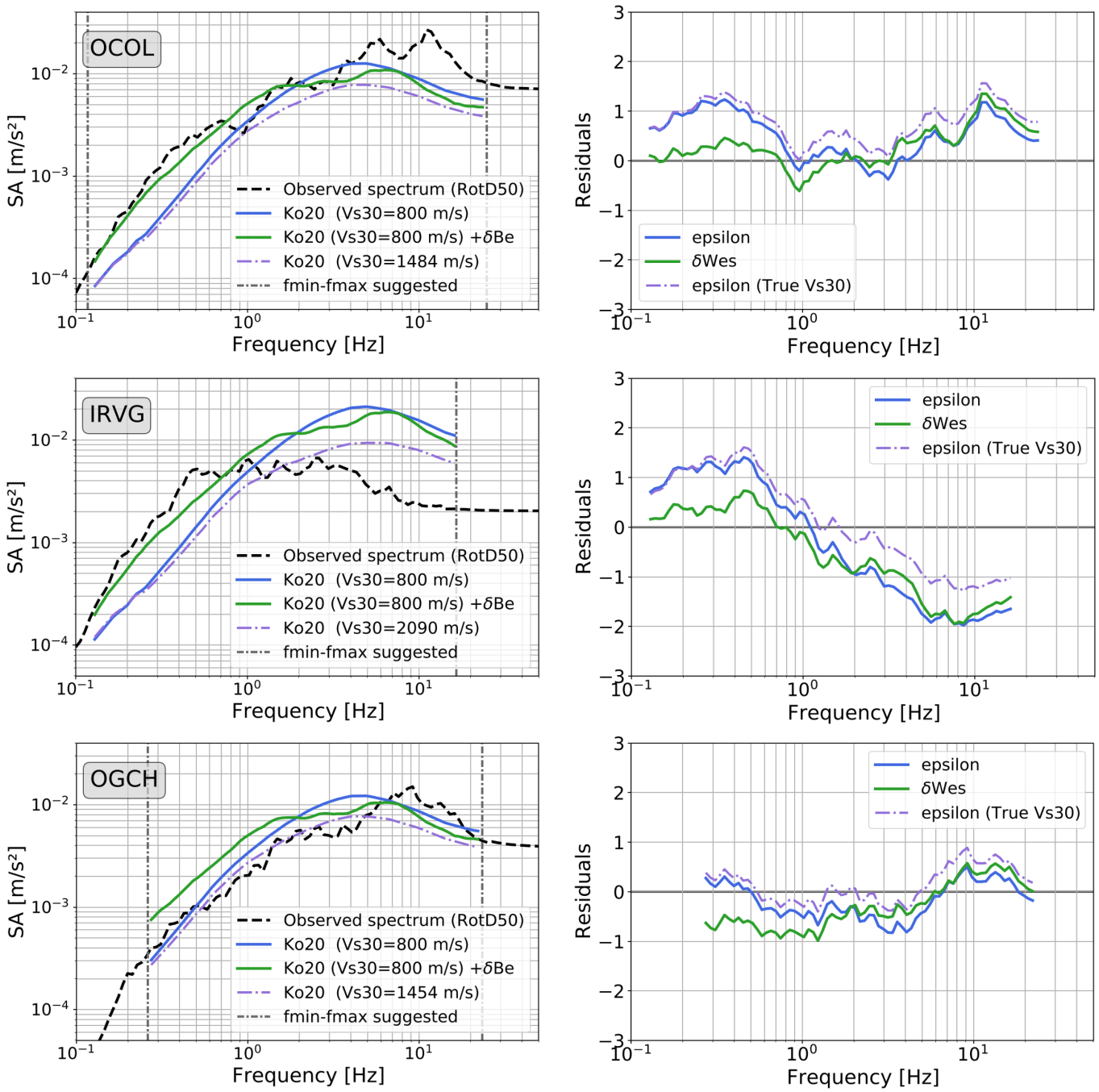

Figure 6 Left panel, comparison between observed (black dashed lines) and predicted spectral accelerations by Ko20's GMM for three representative stations. Spectral accelerations are in m/s^2, with predictions using a fixed V_{S30} value of 800 m/s in blue and predictions corrected for the between-event residual, δB_e, in green. Right panel, display of the corresponding residuals. Blue lines represent the total residual (epsilon), and green lines represent the within-event residual (δW_{es}). The purple dashed lines indicate, for reference, the prediction obtained when the measured V_{S30} value at each station (true V_{S30}) is used in the GMM, along with the corresponding epsilon value. The locations of the three stations are indicated in Figure 2.

less share a common δW_{es} pattern, systematically positive across the entire frequency range (around 1). Several of these stations are located in rather deep sedimentary basins like those of Grenoble (e.g., Guéguen et al., 2007), Nice (e.g., Régnier et al., 2020) or Annecy (e.g., Thouvenot et al., 1998). Their spectral amplitudes are up to ten times higher than the predicted values (see Figure S.14), consistent with findings from other studies (e.g., Courboulex et al., 2013). Another part of the stations from cluster #0 is located in the Rhône Valley. The Rhône Canyon, hundreds of metres deep, is one of the deep canyons formed around the Mediterranean during the Messinian salinity crisis, a major geodynamic event of the Cenozoic (Clauzon, 1982; Do Couto et al., 2024). The strong impedance contrast between the canyon composed of Mesozoic sedimentary series and its thick Plio-Quaternary marly and sandy filling is responsible for site amplification (e.g., Gélis et al., 2022; Froment et al., 2022). The significant amplification at low frequencies is likely due to thick sedimentary fill and strong impedance contrasts, features not accounted for by Ko20 under the assumption of V_{S30} =

800 m/s, and likely not even when using the measured V_{S30} values (see Figure S.14). Assigning a uniform V_{S30} value of 800 m/s to all sites facilitated the identification of sites with strong low-frequency amplification as a distinct cluster. Cluster #0 therefore contains stations strongly affected by local site conditions. These sites are spatially isolated and will not be further discussed in the section 5."Interpretation and Discussion'. A more detailed understanding of the residuals at these sites would require additional V_{S30} measurements, which is beyond the scope of the present study.

In summary, clusters #1 to #3 delineate spatially coherent regions, each anchored by a representative station, and thus can be interpreted as reflecting regional trends in ground motion. At low frequencies, underestimation of GMM predictions is visible around the epicentre, except for the northeast (cluster #1). At higher frequencies, ground motions in the southeast (clusters #1 and #3) are significantly lower than predicted. In the following section, we further investigate the physical explanations for the observed spatial variations in ground motions for clusters #1 to #3, first addressing low-frequency ground motions and then high-frequency ground motions.

5 Interpretation and Discussion

5.1 Underestimation of Low-Frequency Ground Motions

An important outcome of comparing ground motion observations from the Le Teil earthquake with GMM predictions is the systematic underestimation of low-frequency amplitudes (Figure 5). As previously mentioned, the analysis of within-event residuals reveals however that this underestimation is not uniform across the network. It is particularly pronounced in the northwest (OCOL) and southeast (IRVG) directions, while stations in the northeast (such as OGCH, cluster #1) exhibit amplitudes that are closer to the predicted values (Figure 7). The waveform analysis highlights the presence of Rayleigh waves at the OCOL and IRVG stations (Figure 3), where the largest amplitudes generally coincide with their arrival. Additionally, these Rayleigh waves result in bumps in the acceleration response spectra of these two stations, which may be attributed to the presence of Rayleigh waves, which are not captured by the GMM (Figure 6).

Theory indicates that shallow seismic sources are particularly efficient in generating low-frequency surface waves (Aki and Richards, 2002; Rösler and van der Lee, 2020). Large amplitude Rayleigh waves are generally reported in regional records for very shallow earthquakes and explosions (< 3 km) with periods ranging from 0.4 to 2.5 seconds (Båth, 1975; Saikia, 1992; Kafka, 1990). Numerous studies have documented the presence of Rayleigh waves in very shallow earthquakes (depth < 5 km) with M_W between 4.0 and 5.5, across regions such as China (e.g., Luo et al., 2011; Qian et al., 2019; Wang et al., 2023), Australia (Allen, 2020; Allen et al., 2006; Miller et al., 2023; Somerville and Ni, 2010) and Canada (Kim et al., 2006). The shallower the earthquake, the greater the amplitude of Rayleigh waves; if the source is beyond a depth of 5 km, these waves are not visible (Tsai and Aki, 1970; Kafka, 1990). In addition, surface waves such as Rayleigh waves attenuate more slowly with distance than body waves due to their geometric spreading (amplitude decaying as $1/\sqrt{r}$ compared to $1/r$ for body waves) and lower intrinsic attenuation at low frequencies (Aki and Richards, 2002). This slower decay explains why they dominate ground motion at regional distances, particularly for shallow sources where their generation is more efficient.

While the presence of Rayleigh waves thus serves as a reliable indicator of an extremely shallow seismic source, they can be observed only in specific azimuthal directions. Rösler and van der Lee (2020) analysed the radiation patterns of Rayleigh waves considering source depth and frequency. Given the rupture characteristics of the Le Teil earthquake (strike, dip, and rake values of 50°, 45°, and 90°, respectively, Ritz et al., 2020), Rayleigh waves are generated in the northwest and southeast directions, and thus are minimal in the northeast and southwest directions (see Figure S.15). This coincides with the identification of Rayleigh waves at OCOL and IRVG and their absence at OGCH (Figure 3), and more broadly, with distinction of clusters #1, #2, and #3 (Figure 8). Notably, the selected GMMs consistently underestimate low-frequency ground motions at all distances (see Figure 5 and S.6), except in the northeast direction, corresponding to a node in the surface wave radiation pattern (see Figure S.16).

The limitations in current GMMs arise from the databases used in their development (e.g., Ancheta et al., 2014; Lanzano et al., 2019b), which contain few or no earthquakes with extremely shallow depths (< 3 km). In the Ko20 GMM, earthquakes have been classified into three depth categories, including a category for earthquakes with depths less than 10 km. The Ko20 GMM predicts higher amplitudes at short distances (< 30 km) for the 0–10 km depth class than for the 10–20 km depth class across the entire frequency range, particularly at high frequencies (see Figure S.17). According to theoretical expectations, the amplitude of Rayleigh waves is stronger at low frequencies as depth decreases, especially for sources shallower than 5 km (e.g., Saikia, 1992; Kafka, 1990). Besides, since surface waves attenuate more slowly than body waves, they significantly affect ground motions from the source to large distances (see Figure S.6), a feature not currently captured by GMMs. GMMs should therefore treat earthquakes with depths < 5 km as a separate category, even though the available data for this depth range remains limited. To our knowledge, only the Somerville et al. (2009) GMM, developed from extremely shallow earthquakes occurring in Australian cratonic region (a model not tailored to our case study), considers the presence of Rayleigh waves in the response spectrum.

To summarise, a large part of the observed spatial variability at low frequencies is attributed to the radiation pattern of Rayleigh waves generated by this shallow earthquake (1–2 km). Their slower attenuation with distance further amplifies their impact on ground motions, highlighting a gap in current GMMs for shallow

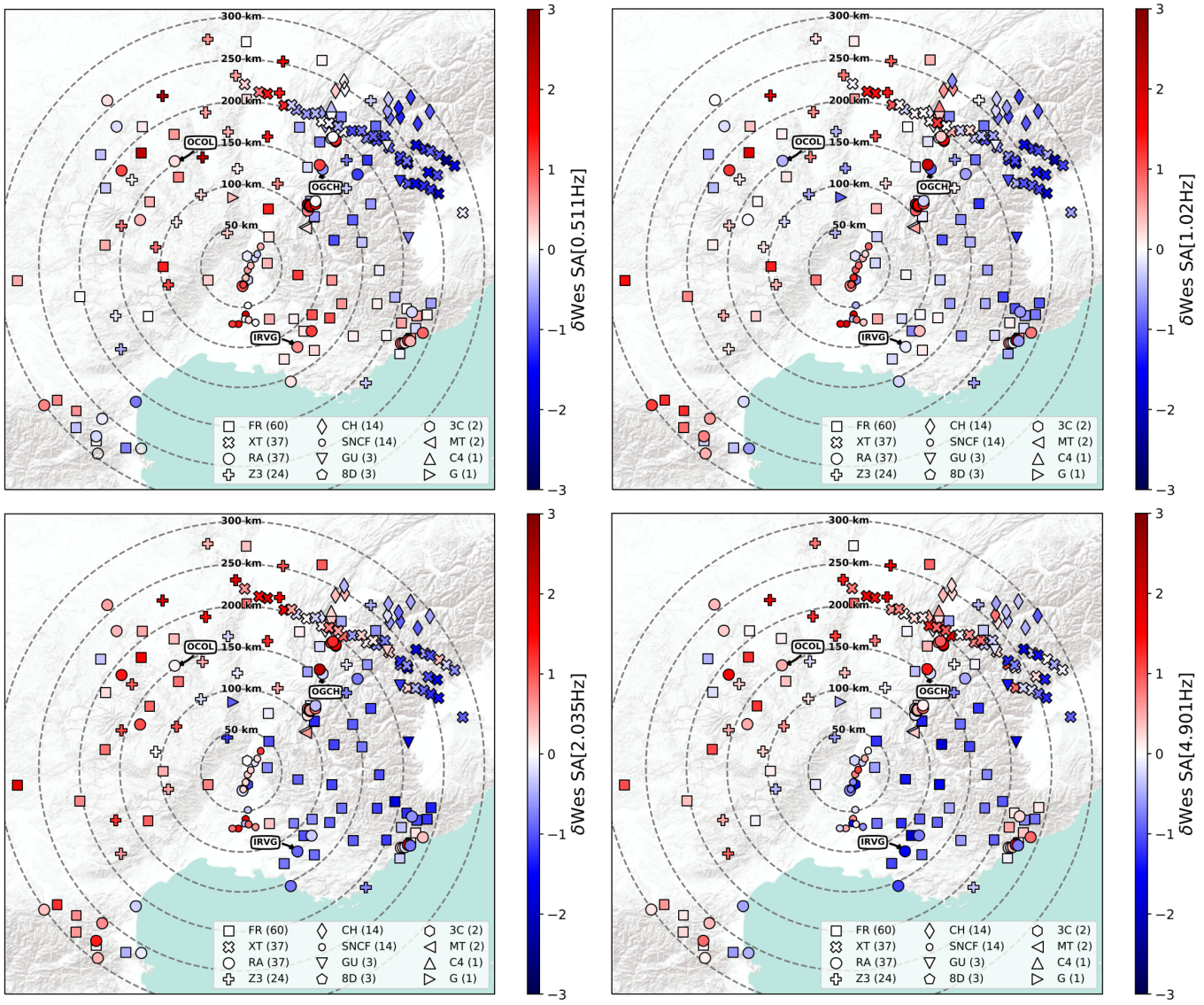

Figure 7 Spatial distribution of within-event residuals (δW_{es}) computed using Ko20's GMM under the assumption of V_{S30}=800 m/s for four frequencies. The colour scale is limited to ±3 to emphasize differences; some data points fall outside these limits.

seismic sources.

5.2 Spatial Variations of High-Frequency Ground Motions

The analysis of within-event residuals revealed clear spatial patterns at high frequencies, in particular faster attenuation of high-frequency ground motions towards the southeast of the rupture (clusters #1 and #3) compared to the northwest (cluster #2) (Figure 8).

It is noteworthy that studies of the Le Teil earthquake source have reported no evidence of rupture directivity (Causse et al., 2021; De Novellis et al., 2020; Delouis et al., 2021), suggesting that the observed azimuthal variations in high-frequency amplitudes should not be attributed to this phenomenon. Additionally, stress drop, a key parameter influencing high-frequency ground motion (e.g., Cotton et al., 2013), was estimated at 1.0 MPa for this earthquake (Causse et al., 2021), which is consistent with the average of worldwide reported stress drops (e.g., Courboulex et al., 2016) and thus unlikely to explain the overall low level of high-frequency ground motion compared to GMMs (Figure 4). As explained in the following, the variations in high-frequency amplitudes observed across the region are likely to be primarily related to wave propagation effects.

Seismic wave attenuation is generally quantified by the quality factor Q. The amplitude of body waves decays as a function of distance r and frequency f according to $exp(-\pi.f.r/c.Q)$, where c is the wave velocity. Seismic attenuation is primarily controlled by two phenomena, including absorption (i.e., the conversion of seismic energy into other forms, e.g., Aki, 1980) and scattering (i.e., the redistribution of seismic energy in the medium due to heterogeneities, inducing a lengthening of the ground motions, e.g., Sato, 1989). Analyses of the quality factor in mainland France reveal frequency and regional variations (Calvet et al., 2013; Campillo and Plantet, 1991; Drouet et al., 2010; Mayor et al., 2018). In particular, Mayor et al. (2018) provided

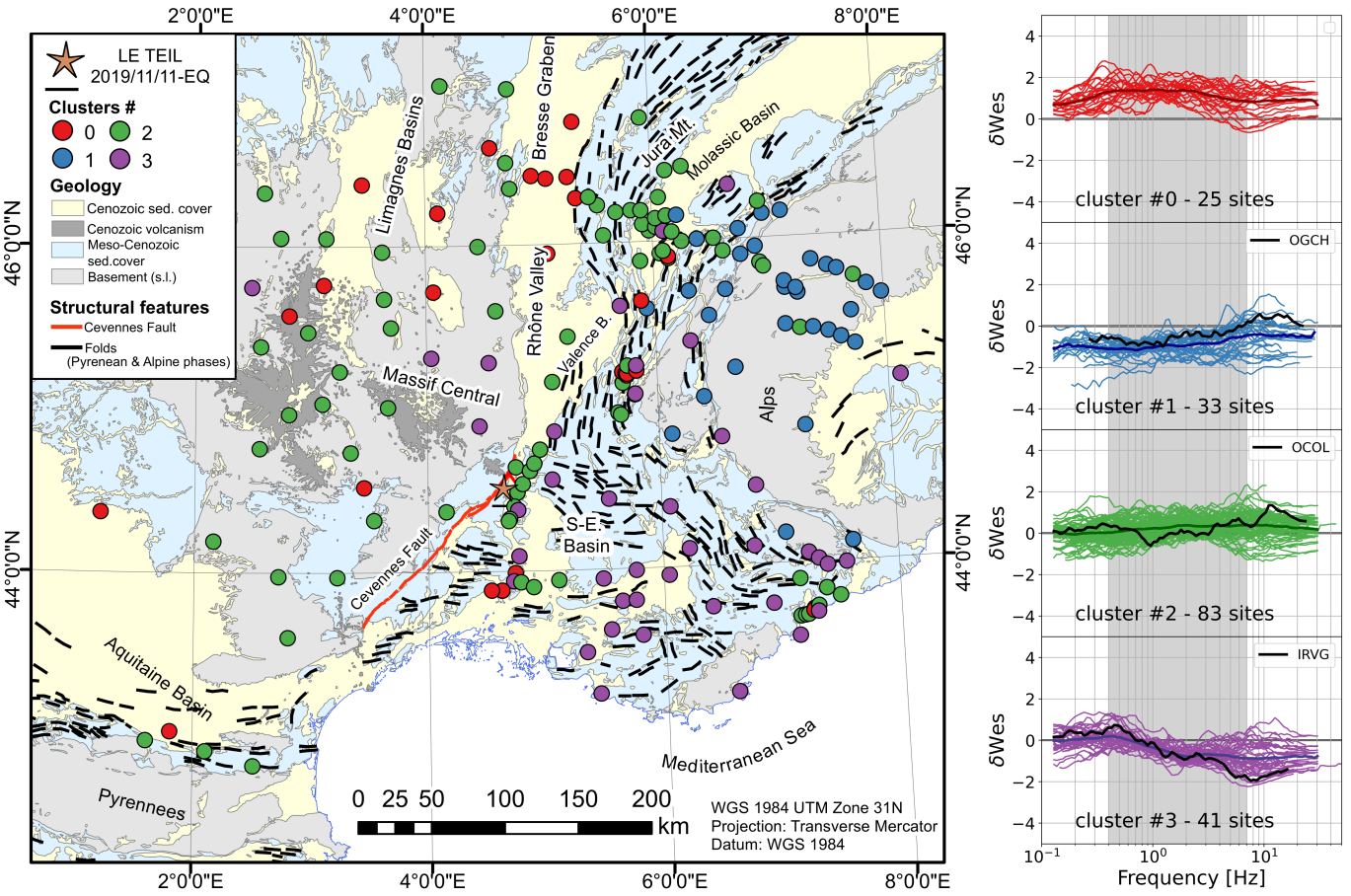

Figure 8 Left panel, spatial distribution of the four clusters identified in this study in relation to simplified geology. Right panel, the δW_{es} values with respect to frequency are depicted for each cluster. The frequency range considered in the clustering analysis (0.4 - 7 Hz) is highlighted in grey. The dark-coloured lines represent the average behaviour of each cluster, while the black lines depict the δW_{es} curves for the three representative stations shown in Figure 6.

an absorption map derived from the coda wave analysis, showing that the southeast region appears to be a strong absorption region across the entire frequency range ($\sim$ 1–30 Hz). Furthermore, a 3-D shear wave velocity model of the Alpine region (Nouibat et al., 2022) indicates significantly lower S-wave velocities in the southeastern basin ($\sim$ 2.7 km/s at 6 km depth) compared to faster velocities west of the Cevennes fault, towards the Massif Central (~ 3.4 km/s). Indeed, the southeast basin region has undergone two phases of compressive deformation due to the Pyrenean and the Alpine orogenies (folding in both directions, see Figure 8). It is, therefore, highly folded and fractured, which could favour scattering and explain the large observed attenuation.

In this section, we also explore another attenuation mechanism through simple numerical simulations. This mechanism, distinct from absorption, is suggested by the combination of specific 1D-features in the velocity structure southeast of Le Teil and the shallow rupture depth.

5.2.1 Local Geological Structure Southeast of Le Teil

We present a simplified cross-section based on geological information obtained from four deep (> 2 km) boreholes located around Le Teil and aligned along a N35° E strike (see Figure 9). The earthquake epicentre is located approximately 2 km southeast of this cross-section. The latter illustrates the main geological layers around the La Rouvière fault and their lateral variations. Causse et al. (2021) produced shear wave velocity (V_S) profiles using a three-component beamforming method (Wathelet et al., 2018), analysing seismic noise recorded at 19 temporary post-seismic stations near the rupture zone (refer to Figure 9 for station locations). This velocity profile indicates an increase in V_S for a layer between approximately 500 and 1000 m depth, followed by a distinct V_S inversion beneath this layer. At greater depths, the velocity profile becomes less constrained. Causse et al. (2021) associated the high V_S value layer with shallow competent limestone units (Berriasian recifal limestone) and marly limestone from the Hauterivian series. The lower V_S layer is linked to softer formations rich in marl from the Late Cretaceous (Valanginian argillaceous limestone). However, it should be noted that the stations used are located between two boreholes, presenting significant lateral variations in the depth of the geological layers. Moreover, the general eastward dip of the geological formations implies that the series identified at the position of the epicentre are probably a little deeper (~200 to 500 m). Finally, the "theoretical" position of the velocity profile is representative of a large volume of the geological series, considering the spatial extension of the seis-

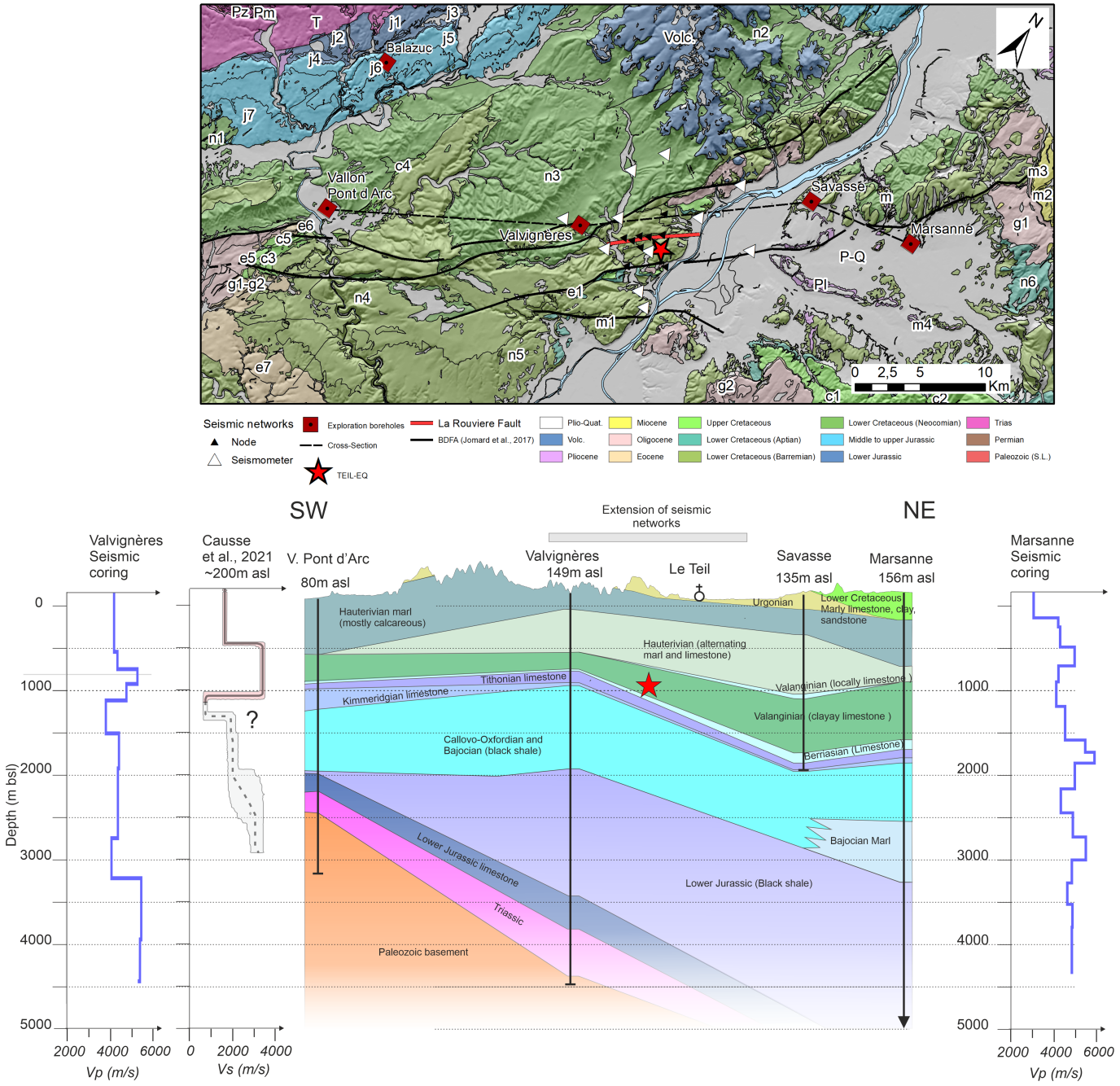

Figure 9 Summary of recent geophysical and geological studies carried out in the vicinity of the hypocentre of the Le Teil earthquake (represented by a red star). In the top panel, a geological map on which the faults are represented by black segments, with the La Rouvière fault highlighted in red. Four boreholes, almost aligned along a NE-trending direction, are represented by red squares (letters and numbers are the uniform notation of series on French geological maps – www.infoterre.fr). Additionally, stations (nodes and seismometers) used to compute the V_S profile by Causse et al. (2021) given below are represented. The pink shape with a solid line corresponds to the part of the profile for which the inversion of the dispersion curves is relatively robust, whereas the shaded part with a dashed line corresponds to a more uncertain result. In the lower panel, a cross-section based on geological information from the four deep boreholes represented by black lines is presented. The colours used in this cross-section correspond to those on the geological map. V_P profiles in blue from the Valvignères and Marsanne boreholes (seismic coring) are given on each side of the cross-section. The V_S profile from Causse et al. (2021) and the corresponding station coverage are indicated on the cross-section (grey rectangle). Geological interfaces and the surface (simplified) are represented in altitude (above or below sea level). Geological information for the boreholes comes from BSS database (www.infoterre.fr). Wells are: Vallon Pont d'Arc (BSS002BMNT), Valvignères (BSS002ARWX), Savasse (BSS002ASEZ) and Marsanne (BSS002ASXR).

mic stations. The one-dimensional hypothesis considered when calculating the dispersion curves is therefore not respected and the representativeness of the column must be considered with caution. Furthermore, seismic coring and sonic measurements conducted at the boreholes provide V_P values (Thomasset et al., 2024).

Figure 9 presents V_P profiles for the Valvignères and Marsanne boreholes. In these V_P profiles, no velocity variation is observed between the Valanginian and Hauterivian series. Higher velocities are found for the Tithonian Kimmeridgian limestones. Deeper, a layer of lower velocity is observed at the level of the Callovo-Oxfordian black shales, which are less competent layers than the overlying limestones. Based on these V_P profiles, the velocity inversion seems more closely related to this black shale series. Defining a velocity profile in this region and correlating it with the local geology remain an open question. Regardless of the geological units associated with this poorly competent layer, the velocity structure of the Le Teil earthquake area is unambiguously characterised by a velocity inversion. We next analyse the effect of the presence of such a layer near the earthquake source on seismic ground motion.

5.2.2 Effect of a Shallow Velocity Inversion on the Ground Motion Decay from Simulations

Here, we conduct numerical simulations to analyse the effect of such a velocity inversion on the decay of ground-motion parameters up to a distance of 50 km. For the sake of simplicity and to better emphasise the involved physical processes, we consider simplified versions of the 1D-velocity profile. This is, of course, a great simplification of the geological complexity of the region. If the low velocity layer is made up of the succession of black shales topped by the Tithonic slab, this simplification has the advantage of considering the continuity of that structure at the scale of the southeast basin which is the reality. However, as the basin deepens rapidly towards its centre, the assumption of a horizontal layer is not very realistic. Furthermore, although the tectonic deformations are not very pronounced to the east of the Cevennes, the same cannot be said for the subalpine ranges, where the layers are highly deformed, bringing to the surface the black shales that are so characteristic of the Baronnies and Diois regions.

We perform ground motion simulations up to a frequency of 5 Hz for two 1D-velocity models (Figure 10). The first model, considered as a reference, consists of a homogeneous half-space overlaid with a 2.5 km-thick layer. In this model, the shallow layer has the lowest V_S value. In contrast, the second model is characterised by a velocity inversion, defined by adding a 1.5 km-thick low-velocity layer buried at 1 km (referred to as LV layer in the following) to the first model. To mimic the source process of the Le Teil event, we use a point source model with (strike, dip, rake) equal to (0°, 45°, 90°). The dip and rake values are consistent with Ritz et al. (2020). The point source is positioned at 0.5 km depth, which roughly corresponds to the depth of the maximum static slip imaged by InSAR data (Cornou et al., 2021). The duration of the source time function is 2 s (Causse et al., 2021) and is represented by a regularised Yoffe function (Tinti et al., 2005). The surface receivers are positioned along a line at epicentral distances from 2 to 50 km, with interstation distance of 2 km up to 20 km and 5 km from 20 to 50 km. Seismograms are obtained by convolving the source time function with Green's functions computed using the discrete wave number technique of Bouchon (1981) (AXITRA computer package, Cotton and Coutant, 1997), for the various 1D-media. The following results are presented for a source-receiver azimuth of 90°, but we have checked that they remain unchanged for azimuths of 45° or 135°. The values of Sa(f) are finally defined as the geometrical mean of spectral acceleration computed on the longitudinal and vertical components.

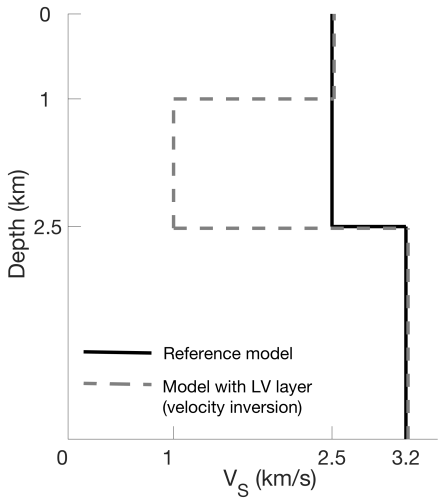

Figure 10 Shear-wave velocity profiles used for the ground motion simulations. The reference model is composed of a homogeneous half space overlaid with a 2.5 km-thick layer. In the second model a low-velocity (LV) layer is introduced, resulting in a velocity inversion. The P-wave velocity is equal to 1.7 V_S.

Figure 11 shows that the decay of Sa(f) with distance is remarkably faster beyond ∼10 km in the presence of a LV layer at 2 Hz and 5 Hz. This is the case considering absorption in the layers (represented by quality factors Q_P and Q_S equal to $V_P/10$ and $V_S/10$, respectively, with V_P and V_S in m/s) or purely elastic medium (infinite quality factors). The mechanisms responsible for such decay are analysed hereafter. In the absence of LV layer, the acceleration time series are dominated by a very weakly dispersive Rayleigh wave propagating at the Rayleigh speed (0.92 V_S), which controls the PGA and results in a short-duration signal (Figure S.18). The presence of a LV layer generates strong later wave arrivals resulting in a drastic increase of the signal duration and significantly smaller peak values (Figure S.18). Such arrivals have a dominant frequency of about 2 Hz (Figure S.19). A snapshot of the velocity particle inside the medium clearly reveals that those late arrivals emanate from the leakage of waves trapped and amplified in the LV layer at the interface between the top and the LV layer (Figure 12). An analysis of the normal modes and dispersion curve of the Rayleigh waves shows that the late arrivals result from the excitation of higher modes (Figure S.20). These simulations are consistent with observations, with lower spectral amplitudes (Figure 3) and longer durations (Figure 2) in the southeast than in the northwest.

We then examine the persistence of the fast decay of

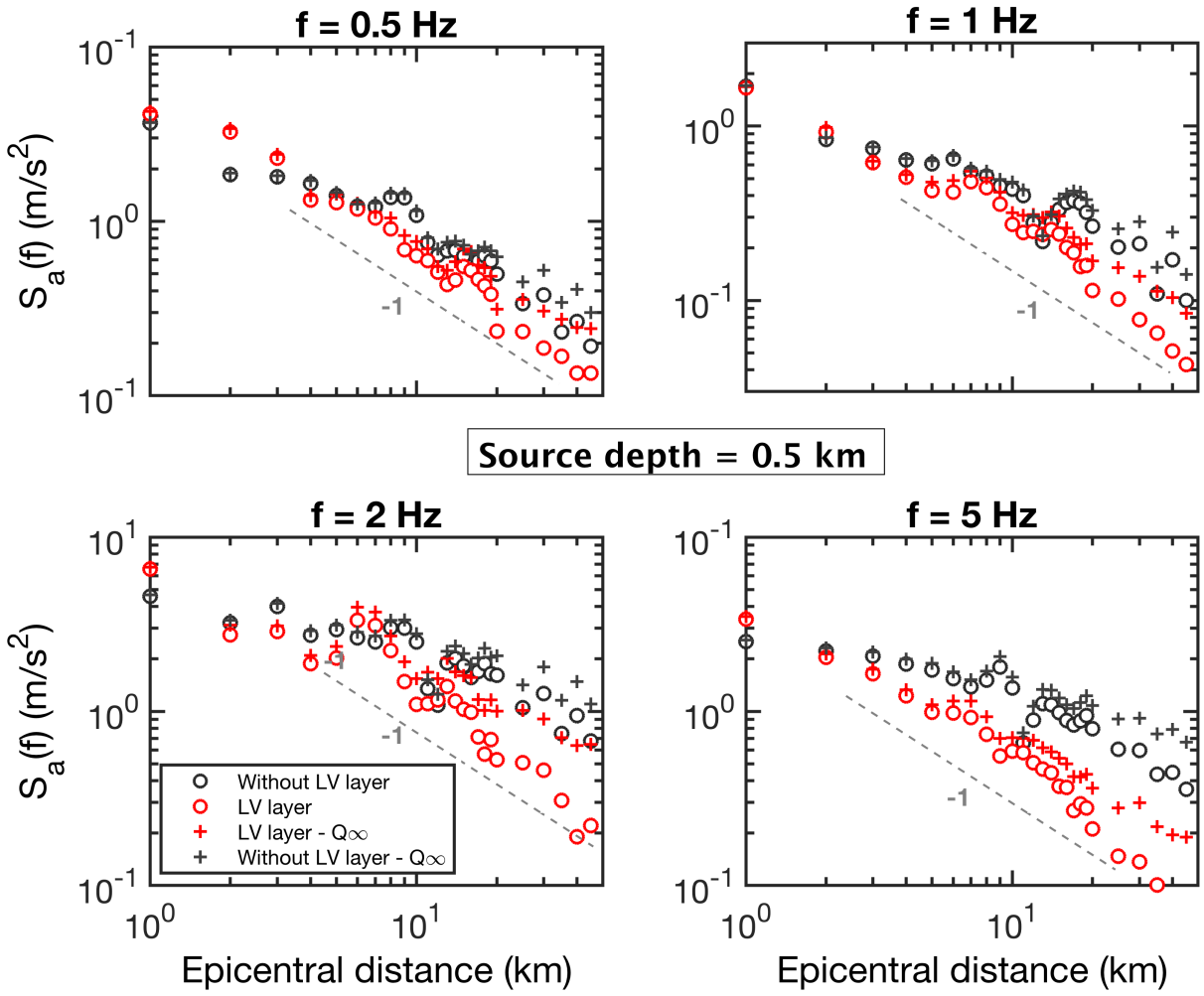

Figure 11 Decrease of spectral acceleration Sa(f) with distance at various frequencies for the 1D-velocity media of Figure 10, that is with the presence of a buried low-velocity (LV) layer (in grey), or without (in red). Sa(f) is computed considering a purely elastic medium (crosses) or with quality factors Q_S and Q_P equal to V_S/10 and V_P/10, respectively (V_S and V_P in m/s).

Sa(f) at 2 and 5 Hz with distance as the LV layer and source properties are varied. Firstly, we also observe a faster decay with distance when the velocity inversion is weaker (V_S=2 km/s in the LV layer instead of V_S=1 km/s). The amplification inside the LV layer is then weaker but it is counterbalanced by a stronger leakage at the top, resulting in similar fast decay of Sa(f) (Figure S.21). Secondly, we verify that the decay persists in the case of a thicker LV layer (2.5 km instead of 1.5 km) and is not sensitive to the dip angle (tested values of 30°, 45° and 60°). It is also poorly sensitive to the source depth as long as the source is located within the surface layer (Figure S.22). However, the fast decay is not observed when the LV layer is buried more than approximately 1.5 km below the surface (Figure S.23). In this case, the amplitude of the late arrivals becomes too weak to control the PGA values (Figure S.24), and the decay of Sa(f) with distance becomes similar with and without the LV layer.

These calculations highlight an additional effective mechanism for the attenuation of high-frequency ground-motion, distinct from classical absorption. Such mechanism may occur when there is a shallow LV layer (above~1.5 km considering our hypotheses) and a shallow source (located above the LV layer). For the shallow Le Teil earthquake, those conditions were likely met southeast of the epicentre. At this moment, it remains however difficult to evaluate the real contribution of this mechanism to the faster high-frequency ground motion amplitude decay observed toward the southeast and up to which distance it may have acted. The assumption of a 1D-velocity model is an oversimplification of the real geological structure at the scale of the southeast basin, which deepens towards the southeast. Further geological and geophysical investigations are necessary to map the geometrical properties of the geological units characterised by low shear-wave velocities. Our simulations indicate that the depth of the top of the low-velocity layers seems to be the most critical property. This can provide insights into the extent of the area on which the approximation of a 1D-velocity model is relevant or help in designing more realistic models (2D).

To summarise, the spatial variability observed at high frequency may be mainly controlled by attenuation mechanisms, including one that could result from the combination between the local velocity properties and the shallow rupture depth.

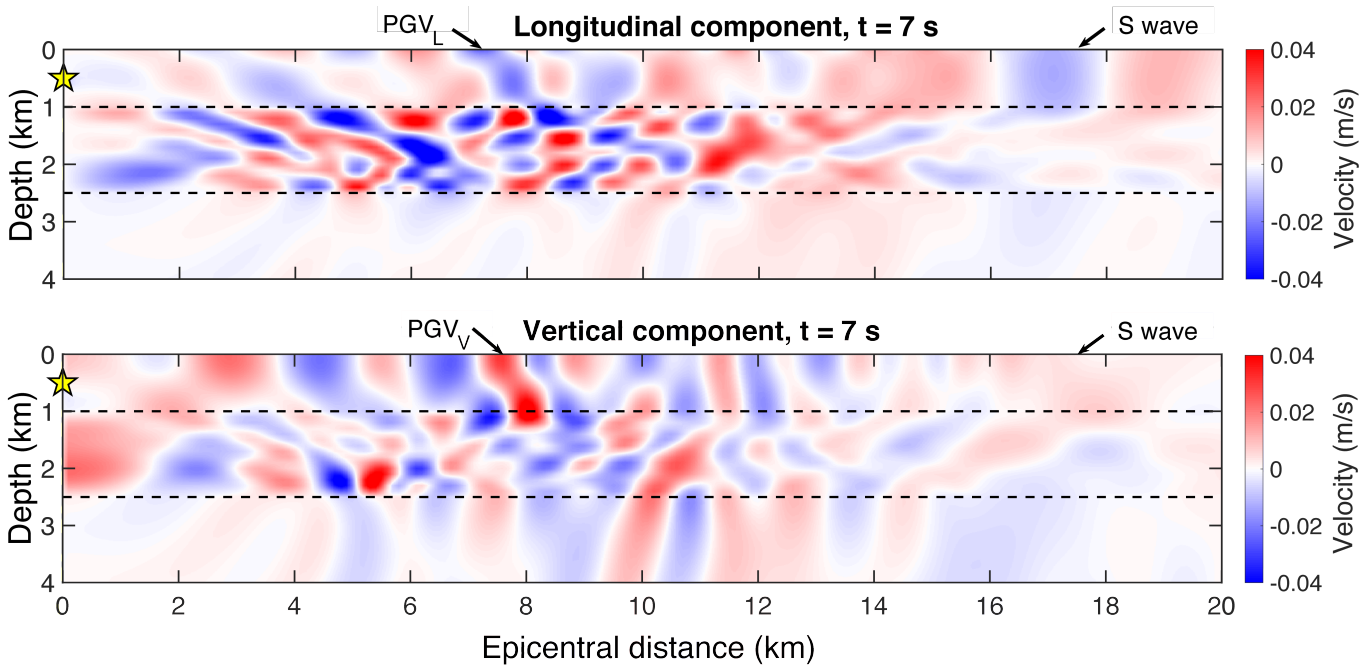

Figure 12 Snapshot at 7s of the particle ground velocity inside the 1D-velocity profile in case of velocity inversion (Figure 10). The LV layer is between the two dashed lines. The Peak Ground Velocity values (PGV) are indicated. The source depth is 0.5 km. The quality factors Q_S and Q_P equal to $V_S/10$ and $V_P/10$, respectively (V_S and V_P in m/s).

6 Conclusions

On 11 November 2019, a moderate M_W 4.9 earthquake occurred at an exceptionally shallow depth (1–2 km) near the town of Le Teil in southeastern France. Numerous good quality ground motion records are available and well distributed around the epicentre (198 stations ranging from 8 to 300 km). Their analysis reveals specific features, including consistent large-scale spatial and frequency-dependent ground motion patterns related to source and path effects. Firstly, at lower frequencies (< 1 Hz), significant Rayleigh waves are generated due to the shallow depth of the rupture, especially in the northwest and southeast directions (orthogonal to the fault direction). In these configurations, various GMMs selected underestimate observations at low frequency across all distances because these waves attenuate less rapidly than body waves. In the northeast direction, which corresponds to a node in the Rayleigh wave radiation pattern, good agreement is observed. Secondly, a clear difference emerges between ground motions in the northwest, characterised by short-duration signals rich in high frequency, and those in the southeast, exhibiting longer durations and high-frequency spectra largely lower than those predicted by GMMs. Several mechanisms may be responsible for this high-frequency attenuation in the southeast. Absorption models, 3-D shear-wave velocity models, and geological evidence of particularly fractured sedimentary formations, support a slower propagation and a faster attenuation of seismic waves in the southeast basin. Furthermore, using simple numerical simulations, we show that the combination of local geological information, including the presence of a low velocity layer beneath the hypocentre, and the extremely shallow depth of the earthquake could be responsible for a faster decay of high-frequency ground motion with distance, and for longer signal durations. To determine whether this significant high-frequency attenuation is specific to the extremely shallow depth of the Le Teil earthquake, or whether it is a regional feature, it would be necessary to carry out a statistical analysis of the Epos-France-RAP and -RLBP dataset of ground motions in mainland France (Traversa et al., 2020; Buscetti et al., 2024). Studies on this subject are currently in progress (Personal communication from S. R. Kotha). Finally, these results still present some limitations, as site conditions are not well constrained and are represented using non-site-specific V_{S30} values (e.g., 800 m/s) in the GMMs. However, several sensitivity tests were performed to support these findings. The clustering analysis also helps to identify stations exhibiting strong low-frequency amplification, particularly in areas with well-documented site effects, such as the Rhône Valley, and the Grenoble and Nice basins. Continued efforts to characterise seismic stations (e.g., Hollender et al., 2018) therefore remain essential to better constrain residual analyses and improve ground motion models.

The Le Teil earthquake is part of a broader context of repeated extremely shallow seismicity in the region. Our analysis demonstrates that GMMs classically used for SHA in mainland France inadequately capture the main ground motion features of the Le Teil earthquake. Improving GMM predictions for extremely shallow earthquakes is essential for accurate seismic hazard assessment in such contexts. This study should be extended to other shallow earthquakes to see if certain systematisms can be found globally. However, identifying such earthquakes in databases can be challenging, as depth is a parameter that is often poorly constrained. Recently, Di et al. (2023) provided an inventory of mod-

Table 2 Main characteristics of the station networks used in this study.

Institutes Projects	FDSN codes	Status	Access	Type of station used	Recording	References
Epos-France	FR	Permanent	Public	HH, HN	Continuous	Epos-France (1995)
	RA	Permanent	Public	HN	Continuous	RESIF (1995)
	MT	Permanent	Public	HH	Continuous	French Landslide Observatory – Seismological Datacenter / RESIF (2006)
	XT	Temporary	Restricted[a]	HH	Continuous	Zhao et al. (2018)
	3C	Temporary	Public	HH, HN	Continuous and triggered	Bertrand et al. (2019)
AlpArray	Z3	Temporary	Restricted[a]	HH	Continuous	AlpArray Seismic Network (2015)
SNCF		Permanent	Restricted	HN	Triggered	Vallage et al. (2021)
GEOSCOPE	G	Permanent	Public	HH, HN	Continuous	Institut de physique du globe de Paris (IPGP) and École et Observatoire des Sciences de la Terre de Strasbourg (EOST) (1982)
SED	CH	Permanent	Public	HH	Continuous	Swiss Seismological Service (SED) At ETH Zurich (1983)
	8D	Temporary	Public	HH	Continuous	Swiss Seismological Service (SED) At ETH Zurich (2005)
	C4	Permanent	Public	HH	Continuous	CERN (2016)
University of Genoa	GU	Permanent	Public	HH	Continuous	University of Genoa (1967)

[a] Access was restricted at the time of the study, and the data are now available via the Epos-France portal.

erate shallow earthquakes associated with surface rupture (earthquakes mainly in China and in Australia) that could have generated significant local damage. Their ground motions could be investigated to improve the seismic hazard of such extremely shallow earthquakes, including Human-induced earthquakes (e.g., Foulger et al., 2018), especially in regions of low-to-moderate seismic activity like mainland France.

Acknowledgments

We thank Anne Paul for the transmission of Le Teil earthquake data from the AlpArray and CIFLAPS-2 projects. These data were under embargo during the project period and have since become publicly available through Epos-France. We also thank Florence Marcilly from SNCF for giving us to the seismic signals of Le Teil earthquake recorded by these stations, as well as CEA for preparing the data and providing information on metadata, with special thanks to Damien Grenié and colleagues. We thank the team «Retour d'expérience post sismique et expérimental pour actualiser les méthodes d'ingénierie conventionnelles» (Post-seismic and Experimental Feedback to Update Conventional Engineering Methods) action within the « Groupe de Gestion de Programme Mécanique des Structures et Séisme" (GGP MSS), more specifically Paola Traversa, for fruitful discussions. The work was partially funded by GGP MSS and the Institute of Research for Development. The authors are grateful to Fabian Bonilla and an anonymous reviewer for their careful reading and comments.

Data and Code Availability

Seismological data are provided by the European Integrated Data Archive (EIDA, http://www.orfeus-eu.org/data/eida/) and the French seismological and geodetic network (Epos-France, https://www.epos-france.fr/). The overall network characteristics and references are described in Table 2. To compute the seismic intensity measures, the Seismic-Intensity-Measure code developed in Python by Maria Lancieri was employed (https://github.com/fiorellalan/Seismic-Intensity-Measure). Data analyses have been performed using both the software python (cartopy, matplotlib, obspy, pandas, scikit-learn, ...) and the software Matlab version R2019A. The basemap is the World Terrain Base map supplied by ArcGIS on this link https://server.arcgisonline.com/arcgis/rest/services/World_Terrain_Base/MapServer. The programs disd3D.exe developed by D. Boore to calculate fault-to-station distances are available online at http://www.daveboore.com/software_online.html (last accessed July 2021). For GMMs, we used the models available in the package gsim of the version 3.13 of openquake. The dataset build during the current study is provided as supplementary material and available on Zenodo (Laurendeau et al., 2024). The Axitra program was used for the numerical simulations.

Competing Interests

The authors have no competing interests.

References

Abrahamson, N. A. and Youngs, R. R. A stable algorithm for regression analyses using the random effects model. *Bulletin of the Seismological Society of America*, 82(1):505–510, Feb. 1992. doi: 10.1785/bssa0820010505.

Aki, K. Scattering and attenuation of shear waves in the lithosphere. *Journal of Geophysical Research: Solid Earth*, 85(B11): 6496–6504, Nov. 1980. doi: 10.1029/jb085ib11p06496.

Aki, K. and Richards, P. *Quantitative seismology*. University Science Books, 2nd edition, 2002.

Al Atik, L., Abrahamson, N., Bommer, J. J., Scherbaum, F., Cotton, F., and Kuehn, N. The Variability of Ground-Motion Prediction Models and Its Components. *Seismological Research Letters*, 81 (5):794–801, Aug. 2010. doi: 10.1785/gssrl.81.5.794.

Allen, T., Dhu, T., Cummins, P., and Schneider, J. Empirical Attenuation of Ground-Motion Spectral Amplitudes in Southwestern Western Australia. *Bulletin of the Seismological Society of America*, 96(2):572–585, Apr. 2006. doi: 10.1785/0120040238.

Allen, T. I. Seismic hazard estimation in stable continental regions: Does PSHA meet the needs for modern engineering design in Australia? *Bulletin of the New Zealand Society for Earthquake Engineering*, 53(1):22–36, Mar. 2020. doi: 10.5459/bnzsee.53.1.22-36.

AlpArray Seismic Network. AlpArray Seismic Network (AASN) temporary component, 2015. doi: 10.12686/ALPARRAY/Z3_2015.

Ampuero, J. P., Audin, L., Bernard, P., Brenguier, F., Delouis, B., Grandin, R., Jolivet, R., Leloup, P. H., Ritz, J., Vergne, J., Vernant, P., and Voisin, C. Rapport d'évaluation du groupe de travail (GT) CNRS-INSU sur le séisme du Teil du 11 novembre 2019 et ses causes possibles. Research report, 2019. https://www.cnrs.fr/sites/default/files/press_info/2019-12/Rapport_GT_Teil_phase1_final_171219_v3.pdf.

Ampuero, J.-P., Billant, J., Brenguier, F., Cavalié, O., Courboulex, F., Deschamps, A., Delouis, B., Grandin, R., Jolivet, R., Liang, C., Mordret, A., and Oral, E. The November 11 2019 Le Teil, France M5 earthquake: a triggered event in nuclear country. Mar. 2020. doi: 10.5194/egusphere-egu2020-18295.

Ancheta, T., Darragh, R., Stewart, J., Seyhan, E., Silva, W., Chiou, B., Wooddell, K., Graves, R., Kottke, A., and Boore, D. PEER NGA-West2 Database. Peer report 2013/03, pacific earthquake engineering research center., University of California, Berkeley, 2013. https://apps.peer.berkeley.edu/publications/peer_reports/reports_2013/webPEER-2013-03-Ancheta.pdf.

Ancheta, T. D., Darragh, R. B., Stewart, J. P., Seyhan, E., Silva, W. J., Chiou, B. S.-J., Wooddell, K. E., Graves, R. W., Kottke, A. R., Boore, D. M., Kishida, T., and Donahue, J. L. NGA-West2 Database. *Earthquake Spectra*, 30(3):989–1005, Aug. 2014. doi: 10.1193/070913eqs197m.

Arthur, D. and Vassilvitskii, S. k-means++: the advantages of careful seeding. In *Proceedings of the Eighteenth Annual ACM-SIAM Symposium on Discrete Algorithms*, SODA '07, page 1027–1035, USA, 2007. Society for Industrial and Applied Mathematics. doi: 10.5555/1283383.1283494.

Assumpção, M., Bianchi, M., Calhau, J., Rosa, D., Baksh, J., Assing, D., Basdeo, C., Zahradnik, J., Dias, F., Jolivet, R., and Calais, E. The 2021 Mw 5.6 Earthquake in the Guyana Shield, South America: An Intraplate Event with No Reason to Occur. *The Seismic Record*, 5(2):228–238, Apr. 2025. doi: 10.1785/0320250002.

Barros, L. V., Assumpção, M., Chimpliganond, C., Carvalho, J. M., Von Huelsen, M. G., Caixeta, D., França, G. S., de Albuquerque, D. F., Ferreira, V. M., and Fontenele, D. P. The Mara Rosa 2010 GT-5 earthquake and its possible relationship with the continental-scale transbrasiliano lineament. *Journal of South American Earth Sciences*, 60:1–9, July 2015. doi: 10.1016/j.jsames.2015.02.002.

Beauval, C., Bard, P.-Y., and Danciu, L. The influence of source- and ground-motion model choices on probabilistic seismic hazard levels at 6 sites in France. *Bulletin of Earthquake Engineering*, 18 (10):4551–4580, June 2020. doi: 10.1007/s10518-020-00879-z.

Bertrand, E., Cornou, C., Gélis, C., Rivet, D., and SISMOB-RESIF. Le Teil P5 post seismic experiment, 2019. doi: 10.15778/RESIF.3C2019.

Bindi, D., Massa, M., Luzi, L., Ameri, G., Pacor, F., Puglia, R., and Augliera, P. Pan-European ground-motion prediction equations for the average horizontal component of PGA, PGV, and 5 to 3.0 s using the RESORCE dataset. *Bulletin of Earthquake Engineering*, 12(1):391–430, Nov. 2014. doi: 10.1007/s10518-013-9525-5.

Bindi, D., Spallarossa, D., and Pacor, F. Between-event and between-station variability observed in the Fourier and response spectra domains: comparison with seismological models. *Geophysical Journal International*, 210(2):1092–1104, May 2017. doi: 10.1093/gji/ggx217.

Bollinger, L., Nicolas, M., and Marin, S. Hydrological triggering of the seismicity around a salt diapir in Castellane, France. *Earth and Planetary Science Letters*, 290(1–2):20–29, Feb. 2010. doi: 10.1016/j.epsl.2009.11.051.

Bollinger, L., Le Dortz, K., Duverger, C., Vallage, A., Marin, S., and Leroy, Y. M. Seismic swarms in Tricastin, lower Rhône Valley (France): review of historical and instrumental seismicity and models. *Comptes Rendus. Géoscience*, 353(S1):585–606, Jan. 2021. doi: 10.5802/crgeos.93.

Bommer, J. J., Stafford, P. J., and Alarcon, J. E. Empirical Equations for the Prediction of the Significant, Bracketed, and Uniform Duration of Earthquake Ground Motion. *Bulletin of the Seismological Society of America*, 99(6):3217–3233, Nov. 2009. doi: 10.1785/0120080298.

Boore, D. M. Orientation-Independent, Nongeometric-Mean Measures of Seismic Intensity from Two Horizontal Components of Motion. *Bulletin of the Seismological Society of America*, 100(4): 1830–1835, July 2010. doi: 10.1785/0120090400.

Boore, D. M., Stewart, J. P., Seyhan, E., and Atkinson, G. M. NGA-West2 Equations for Predicting PGA, PGV, and 5% Damped PSA for Shallow Crustal Earthquakes. *Earthquake Spectra*, 30(3): 1057–1085, 08 2014. doi: 10.1193/070113EQS184M.

Bouchon, M. A simple method to calculate Green's functions for elastic layered media. *Bulletin of the Seismological Society of America*, 71(4):959–971, Aug. 1981. doi: 10.1785/bssa0710040959.

Burnol, A., Armandine Les Landes, A., Raucoules, D., Foumelis, M., Allanic, C., Paquet, F., Maury, J., Aochi, H., Guillon, T., Delatre, M., Dominique, P., Bitri, A., Lopez, S., Pébaÿ, P. P., and Bazargan-Sabet, B. Impacts of Water and Stress Transfers from Ground Surface on the Shallow Earthquake of 11 November 2019 at Le Teil (France). *Remote Sensing*, 15(9):2270, Apr. 2023. doi: 10.3390/rs15092270.

Buscetti, M., Traversa, P., Perron, V., Rischette, P., Hollender, F., and Shible, H. Epos-France Database of Earthquake Ground Motion for Mainland France: 1996–2021 Updated Version. *Seismological Research Letters*, 96(2A):1214–1226, Sept. 2024. doi: 10.1785/0220240053.

Båth, M. Short-period Rayleigh waves from near-surface events. *Physics of the Earth and Planetary Interiors*, 10(4):369–376, Aug. 1975. doi: 10.1016/0031-9201(75)90064-3.

Cadet, H., Bard, P.-Y., and Rodriguez-Marek, A. Defining a Standard Rock Site: Propositions Based on the KiK-net Database. *Bulletin of the Seismological Society of America*, 100(1):172–195, Jan. 2010. doi: 10.1785/0120090078.

Calvet, M., Sylvander, M., Margerin, L., and Villaseñor, A. Spatial variations of seismic attenuation and heterogeneity in the Pyrenees: Coda Q and peak delay time analysis. *Tectonophysics*, 608: 428–439, Nov. 2013. doi: 10.1016/j.tecto.2013.08.045.

Campillo, M. and Plantet, J. Frequency dependence and spatial distribution of seismic attenuation in France: experimental results and possible interpretations. *Physics of the Earth and Planetary Interiors*, 67(1–2):48–64, May 1991. doi: 10.1016/0031-9201(91)90059-q.

Castellaro, S., Mulargia, F., and Rossi, P. L. Vs30: Proxy for Seismic Amplification? *Seismological Research Letters*, 79(4):540–543, July 2008. doi: 10.1785/gssrl.79.4.540.

Causse, M., Cornou, C., Maufroy, E., Grasso, J.-R., Baillet, L., and El Haber, E. Exceptional ground motion during the shallow Mw 4.9 2019 Le Teil earthquake, France. *Communications Earth & Environment*, 2(1), Jan. 2021. doi: 10.1038/s43247-020-00089-0.

Cauzzi, C., Faccioli, E., Vanini, M., and Bianchini, A. Updated predictive equations for broadband (0.01–10 s) horizontal response spectra and peak ground motions, based on a global dataset of digital acceleration records. *Bulletin of Earthquake Engineering*, 13(6):1587–1612, Oct. 2015. doi: 10.1007/s10518-014-9685-y.

CERN. CERN Seismic Network, 2016. doi: 10.12686/SED/NETWORKS/C4.

Chiou, B. S.-J. and Youngs, R. R. Update of the Chiou and Youngs NGA Model for the Average Horizontal Component of Peak Ground Motion and Response Spectra. *Earthquake Spectra*, 30(3):1117–1153, Aug. 2014. doi: 10.1193/072813eqs219m.

Clauzon, G. Le canyon messinien du Rhone; une preuve decive du "desiccated deep-basin model" (Hsue, Cita and Ryan, 1973). *Bulletin de la Société Géologique de France*, S7-XXIV(3):597–610, Jan. 1982. doi: 10.2113/gssgfbull.s7-xxiv.3.597.

Cornou, C., Ampuero, J.-P., Aubert, C., Audin, L., Baize, S., Billant, J., Brenguier, F., Causse, M., Chlieh, M., Combey, A., de Michele, M., Delouis, B., Deschamps, A., Ferry, M., Foumelis, M., Froment, B., Gélis, C., Grandin, R., Grasso, J.-R., Hannouz, E., Hok, S., Jung, A., Jolivet, R., Langlais, M., Langlaude, P., Larroque, C., Leloup, P. H., Manchuel, K., Marconato, L., Maron, C., Mathot, E., Maufroy, E., Mercerat, D., Metois, M., Nayman, E., Pondaven, I., Provost, L., Régnier, J., Ritz, J.-F., Rivet, D., Schlupp, A., Sladen, A., Voisin, C., Walpersdorf, A., Wolynieck, D., Allemand, P., Beck, E., Bertrand, E., Bertrand, V., Briole, P., Brunel, D., Cavalié, O., Chèze, J., Courboulex, F., Douste-Bacque, I., Dretzen, R., Giampietro, T., Godano, M., Grandjean, P., Grunberg, M., Guerin, G., Guillot, S., Haber, E. E., Hernandez, A., Jomard, H., Lasserre, C., Liang, C., Lior, I., Martin, X., Mata, D., Menager, M., Mercier, A., Mordret, A., Oral, E., Paul, A., Peix, F., Pequegnat, C., Pernoud, M., Satriano, C., Sassi, R., Schaming, M., Sellier, V., Sira, C., Socquet, A., Sue, C., Trilla, A., Vallée, M., van den Ende, M., Vernant, P., Vial, B., and Weng, H. Rapid response to the Mw 4.9 earthquake of November 11, 2019 in Le Teil, Lower Rhône Valley, France. *Comptes Rendus. Géoscience*, 353(S1):441–463, 2021. doi: 10.5802/crgeos.30.

Cotton, F. and Coutant, O. Dynamic stress variations due to shear faults in a plane-layered medium. *Geophysical Journal International*, 128(3):676–688, Mar. 1997. doi: 10.1111/j.1365-246x.1997.tb05328.x.

Cotton, F., Archuleta, R., and Causse, M. What is Sigma of the Stress Drop? *Seismological Research Letters*, 84(1):42–48, Jan. 2013. doi: 10.1785/0220120087.

Courboulex, F., Dujardin, A., Vallee, M., Delouis, B., Sira, C., Deschamps, A., Honore, L., and Thouvenot, F. High-Frequency Directivity Effect for an Mw 4.1 Earthquake, Widely Felt by the Population in Southeastern France. *Bulletin of the Seismological Society of America*, 103(6):3347–3353, Nov. 2013. doi: 10.1785/0120130073.

Courboulex, F., Vallée, M., Causse, M., and Chounet, A. Stress-Drop Variability of Shallow Earthquakes Extracted from a Global Database of Source Time Functions. *Seismological Research Letters*, 87(4):912–918, May 2016. doi: 10.1785/0220150283.

Danciu, L., Nandan, S., Reyes, C., Basili, R., Weatherill, G., Beauval, C., Rovida, A., Vilanova, S., Sesetyan, K., Bard, P.-Y., Cotton, F., Wiemer, S., and Giardini, D. The 2020 update of the European Seismic Hazard Model - ESHM20: Model Overview, 2021. doi: 10.12686/A15.

De Novellis, V., Convertito, V., Valkaniotis, S., Casu, F., Lanari, R., Monterroso Tobar, M. F., and Pino, N. A. Coincident locations of rupture nucleation during the 2019 Le Teil earthquake, France and maximum stress change from local cement quarrying. *Communications Earth & Environment*, 1(1):20, 2020. doi: https://doi.org/10.1038/s43247-020-00021-6.

Delouis, B., Oral, E., Menager, M., Ampuero, J.-P., Guilhem Trilla, A., Régnier, M., and Deschamps, A. Constraining the point source parameters of the 11 November 2019 Mw 4.9 Le Teil earthquake using multiple relocation approaches, first motion and full waveform inversions. *Comptes Rendus. Géoscience*, 353 (S1):493–516, Jan. 2021. doi: 10.5802/crgeos.78.

Di, N., Li, C., Li, T., Hu, W., Chen, Z., Zhang, Y., Lü, L., Chen, J., and Shan, X. The 2021 Mw 5.2 Baicheng Earthquake: Implications for the Hazards of Extremely Shallow Earthquakes. *Seismological Research Letters*, Apr. 2023. doi: 10.1785/0220220328.

Do Couto, D., Cushing, E. M., Mocochain, L., Rubino, J.-L., Miquelis, F., Hanot, F., Froment, B., Gélis, C., Camus, H., Bagayoko, N., and Bellier, O. Messinian canyons morphology of the Rhône and Ardèche rivers (south-east France): new insights from seismic profiles. *BSGF - Earth Sciences Bulletin*, 195:19, 2024. doi: 10.1051/bsgf/2024015.

Drouet, S., Cotton, F., and Guéguen, P. VS30, κ, regional attenuation and Mw from accelerograms: Application to magnitude 3–5 French earthquakes. *Geophysical Journal International*, 182(2): 880–898, May 2010. doi: 10.1111/j.1365-246x.2010.04626.x.

Epos-France. EPOS-France-RLBP French Broad-band network, EPOS-France-RAP strong motion network and other seismic stations in metropolitan France [Data set, 1995. doi: 10.15778/RESIF.FR.

Foulger, G. R., Wilson, M. P., Gluyas, J. G., Julian, B. R., and Davies, R. J. Global review of human-induced earthquakes. *Earth-Science Reviews*, 178:438–514, Mar. 2018. doi: 10.1016/j.earscirev.2017.07.008.

French Landslide Observatory – Seismological Datacenter / RESIF. Observatoire Multi-disciplinaire des Instabilités de Versants (OMIV). Résif—Réseau Sismologique et géodésique Français, 2006. doi: 10.15778/RESIF.MT.

Froment, B., Olivar-Castaño, A., Ohrnberger, M., Gisselbrecht, L., Hannemann, K., Cushing, E. M., Boué, P., Gélis, C., Haendel, A., Pilz, M., Hillmann, L., Barbaux, O., Beauprêtre, S., Bouzat, G., Chaljub, E., Cotton, F., Lavoué, F., Stehly, L., Zhu, C., Magnin, O., Métral, L., Mordret, A., Richet, Y., and Tourette, A. Complementary Dense Datasets Acquired in a Low-to-Moderate Seismicity Area for Characterizing Site Effects: Application in the French Rhône Valley. *Seismological Research Letters*, 94(1):531–547, Nov. 2022. doi: 10.1785/0220220244.

Guéguen, P., Cornou, C., Garambois, S., and Banton, J. On the Limitation of the H/V Spectral Ratio Using Seismic Noise as an Exploration Tool: Application to the Grenoble Valley (France), a Small Apex Ratio Basin. *Pure and Applied Geophysics*, 164(1):115–134, Jan 2007. doi: 10.1007/s00024-006-0151-x.

Gélis, C., Cauchie, L., Cushing, E. M., Froment, B., Franco, S., Jomard, H., Moiriat, D., Provost, L., Sariguzel, B., and Tebib, H. Estimation of the Local Seismic Amplification on an Industrialized Site in the French Rhône Valley. *Pure and Applied Geophysics*, 179(6–7):2119–2145, July 2022. doi: 10.1007/s00024-022-03069-x.

Hetényi, G., Molinari, I., Clinton, J., Bokelmann, G., Bondár, I., Crawford, W. C., Dessa, J.-X., Doubre, C., Friederich, W., Fuchs, F., Giardini, D., Gráczer, Z., Handy, M. R., Herak, M., Jia, Y., Kissling, E., Kopp, H., Korn, M., Margheriti, L., Meier, T., Mucciarelli, M.,

Paul, A., Pesaresi, D., Piromallo, C., Plenefisch, T., Plomerová, J., Ritter, J., Rümpker, G., Šipka, V., Spallarossa, D., Thomas, C., Tilmann, F., Wassermann, J., Weber, M., Wéber, Z., Wesztergom, V., and Živčić, M. The AlpArray Seismic Network: A Large-Scale European Experiment to Image the Alpine Orogen. *Surveys in Geophysics*, 39(5):1009–1033, Apr. 2018. doi: 10.1007/s10712-018-9472-4.

Hollender, F., Cornou, C., Dechamp, A., Oghalaei, K., Renalier, F., Maufroy, E., Burnouf, C., Thomassin, S., Wathelet, M., Bard, P.-Y., Boutin, V., Desbordes, C., Douste-Bacqué, I., Foundotos, L., Guyonnet-Benaize, C., Perron, V., Régnier, J., Roullé, A., Langlais, M., and Sicilia, D. Characterization of site conditions (soil class, VS30, velocity profiles) for 33 stations from the French permanent accelerometric network (RAP) using surface-wave methods. *Bulletin of Earthquake Engineering*, 16(6): 2337–2365, 2018. doi: 10.1007/s10518-017-0135-5.

Hollender, F., Roumelioti, Z., Maufroy, E., Traversa, P., and Mariscal, A. Can We Trust High-Frequency Content in Strong-Motion Database Signals? Impact of Housing, Coupling, and Installation Depth of Seismic Sensors. *Seismological Research Letters*, 91(4):2192–2205, May 2020. doi: 10.1785/0220190163.

Institut de physique du globe de Paris (IPGP) and École et Observatoire des Sciences de la Terre de Strasbourg (EOST). Institut de physique du globe de Paris (IPGP) and Ecole et Observatoire des Sciences de la Terre de Strasbourg (EOST, 1982. doi: 10.18715/GEOSCOPE.G.

Jain, A. K. Data clustering: 50 years beyond K-means. *Pattern Recognition Letters*, 31(8):651–666, June 2010. doi: 10.1016/j.patrec.2009.09.011.

Jomard, H., Scotti, O., Auclair, S., Dominique, P., Manchuel, K., and Sicilia, D. The SISFRANCE database of historical seismicity. State of the art and perspectives. *Comptes Rendus. Géoscience*, 353 (S1):257–280, 2021. doi: 10.5802/crgeos.91.

Kafka, A. Rg as a depth discriminant for earthquakes and explosions : A case study in New England. *Bulletin of the Seismological Society of America*, 80(2):373–394, 1990. doi: 10.1785/BSSA0800020373.

Kim, W.-Y., Dineva, S., Ma, S., and Eaton, D. The 4 August 2004, Lake Ontario, Earthquake. *Seismological Research Letters*, 77 (1):65–73, Jan. 2006. doi: 10.1785/gssrl.77.1.65.

Kotha, S. R., Weatherill, G., Bindi, D., and Cotton, F. A regionally-adaptable ground-motion model for shallow crustal earthquakes in Europe. *Bulletin of Earthquake Engineering*, 18(9): 4091–4125, May 2020. doi: 10.1007/s10518-020-00869-1.

Kotha, S. R., Weatherill, G., Bindi, D., and Cotton, F. Near-source magnitude scaling of spectral accelerations: analysis and update of Kotha et al. (2020) model. *Bulletin of Earthquake Engineering*, 20(3):1343–1370, Jan. 2022. doi: 10.1007/s10518-021-01308-5.

Lanzano, G., Luzi, L., Pacor, F., Felicetta, C., Puglia, R., Sgobba, S., and D'Amico, M. A Revised Ground-Motion Prediction Model for Shallow Crustal Earthquakes in Italy. *Bulletin of the Seismological Society of America*, 109(2):525–540, Feb. 2019a. doi: 10.1785/0120180210.

Lanzano, G., Sgobba, S., Luzi, L., Puglia, R., Pacor, F., Felicetta, C., D'Amico, M., Cotton, F., and Bindi, D. The pan-European Engineering Strong Motion (ESM) flatfile: compilation criteria and data statistics. *Bulletin of Earthquake Engineering*, 17(2): 561–582, 2019b. doi: 10.1007/s10518-018-0480-z.

Larroque, C., Baize, S., Albaric, J., Jomard, H., Trévisan, J., Godano, M., Cushing, M., Deschamps, A., Sue, C., Delouis, B., Potin, B., Courboulex, F., Régnier, M., Rivet, D., Brunel, D., Chèze, J., Martin, X., Maron, C., and Peix, F. Seismotectonics of south-east France: from the Jura mountains to Corsica. *Comptes Rendus. Géoscience*, 353(S1):105–151, Jan. 2021. doi: 10.5802/crgeos.69.

Laurendeau, A., Causse, M., Cushing, E. M., Gélis, C., Lancieri, M., Rusch, R., Fahed, P., Cornou, C., and Hok, S. Dataset of: The extremely shallow Mw 4.9 2019 Le Teil earthquake, France: main ground motion features and comparison with ground motion models, Jan. 2024. doi: 10.5281/zenodo.10462970.

Lemoine, A., Douglas, J., and Cotton, F. Testing the Applicability of Correlations between Topographic Slope and VS30 for Europe. *Bulletin of the Seismological Society of America*, 102(6): 2585–2599, Dec. 2012. doi: 10.1785/0120110240.

Luo, Y., Ni, S., Zeng, X., Xie, J., Chen, Y., and Long, F. The M5.0 Suining-Tongnan (China) earthquake of 31 January 2010: A destructive earthquake occurring in sedimentary cover. *Chinese Science Bulletin*, 56(6):521–525, Feb. 2011. doi: 10.1007/s11434-010-4276-2.

Mayor, J., Traversa, P., Calvet, M., and Margerin, L. Tomography of crustal seismic attenuation in Metropolitan France: implications for seismicity analysis. *Bulletin of Earthquake Engineering*, 16(6):2195–2210, Apr. 2018. doi: 10.1007/s10518-017-0124-8.

Miller, M. S., Pickle, R., Murdie, R., Yuan, H., Allen, T. I., Gessner, K., Kennett, B. L. N., and Whitney, J. Southwest Australia Seismic Network (SWAN): Recording Earthquakes in Australia's Most Active Seismic Zone. *Seismological Research Letters*, 94(2A): 999–1011, Jan. 2023. doi: 10.1785/0220220323.

Nouibat, A., Stehly, L., Paul, A., Schwartz, S., Bodin, T., Dumont, T., Rolland, Y., Brossier, R., and AlpArray Working Group, C. Lithospheric transdimensional ambient-noise tomography of W-Europe: implications for crustal-scale geometry of the W-Alps. *Geophysical Journal International*, 229(2):862–879, 2022. doi: 10.1093/gji/ggab520.

Oth, A., Miyake, H., and Bindi, D. On the relation of earthquake stress drop and ground motion variability. *Journal of Geophysical Research: Solid Earth*, 122(7):5474–5492, July 2017. doi: 10.1002/2017jb014026.

Qian, Y., Chen, X., Luo, H., Wei, S., Wang, T., Zhang, Z., and Luo, X. An Extremely Shallow Mw4.1 Thrust Earthquake in the Eastern Sichuan Basin (China) Likely Triggered by Unloading During Infrastructure Construction. *Geophysical Research Letters*, 46(23): 13775–13784, Dec. 2019. doi: 10.1029/2019gl085199.

Regnier, J., Laurendeau, A., Duval, A., and Gueguen, P. From heterogeneous set of soil data to VS profile: Application on the French accelerometric network (RAP) sites. In *14th European conference on earthquake engineering*, 2010.

RESIF. Epos-France RAP French Accelerometric Network [Data set]. RESIF – Réseau Sismologique et géodésique Français, 1995. doi: 10.15778/RESIF.RA.

Ritz, J.-F., Baize, S., Ferry, M., Larroque, C., Audin, L., Delouis, B., and Mathot, E. Surface rupture and shallow fault reactivation during the 2019 Mw 4.9 Le Teil earthquake, France. *Communications Earth & Environment*, 1(1), Aug. 2020. doi: 10.1038/s43247-020-0012-z.

Régnier, J., Bertrand, E., and Cadet, H. Repeatable process for seismic microzonation using 1-D site-specific response spectra assessment approaches. Application to the city of Nice, France. *Engineering Geology*, 270:105569, June 2020. doi: 10.1016/j.enggeo.2020.105569.

Rösler, B. and van der Lee, S. Using Seismic Source Parameters to Model Frequency-Dependent Surface-Wave Radiation Patterns. *Seismological Research Letters*, 91(2A):992–1002, Jan. 2020. doi: 10.1785/0220190128.

Saikia, C. K. Numerical study of quarry generated Rg as a discriminant for earthquakes and explosions: Modeling of Rg in south-western New England. *Journal of Geophysical Research: Solid*

Earth, 97(B7):11057–11072, July 1992. doi: 10.1029/92jb00621.

Sato, H. Broadening of seismogram envelopes in the randomly inhomogeneous lithosphere based on the parabolic approximation: southeastern Honshu, Japan. *Journal of Geophysical Research: Solid Earth*, 94(B12):17735–17747, Dec. 1989. doi: 10.1029/jb094ib12p17735.

Schlupp, A., Sira, C., Maufroy, E., Provost, L., Dretzen, R., Bertrand, E., Beck, E., and Schaming, M. EMS98 intensities distribution of the "Le Teil" earthquake, France, 11 November 2019 (Mw 4.9) based on macroseismic surveys and field investigations. *Comptes Rendus. Géoscience*, 353(S1):465–492, 2021. doi: 10.5802/crgeos.88.

Scotti, O., Baumont, D., Quenet, G., and Levret, A. The French macroseismic database SISFRANCE: objectives, results and perspectives. *Annals of Geophysics*, 47(2–3), 2004. doi: 10.4401/ag-3323.

Somerville, P. and Ni, S. Contrast in seismic wave propagation and ground motion models between cratonic and other regions of Australia. In *Australian Earthquake Engineering Society 2010 Conference*, Perth, Western Australia, 2010.

Somerville, P., Graves, R., Collins, N., Song, S., Ni, S., and Cummins, P. Source and ground motion models for Australian earthquakes. In *Proc. 2009 Annual Conference of the Australian Earthquake Engineering Society*, pages 11––13, 2009.

Stockwell, R., Mansinha, L., and Lowe, R. Localization of the complex spectrum: the S transform. *IEEE Transactions on Signal Processing*, 44(4):998–1001, Apr. 1996. doi: 10.1109/78.492555.

Swiss Seismological Service (SED) At ETH Zurich. National Seismic Networks of Switzerland, 1983. doi: 10.12686/SED/NETWORKS/CH.

Swiss Seismological Service (SED) At ETH Zurich. Temporary deployments in Switzerland associated with aftershocks and other seismic sequences, 2005. doi: 10.12686/SED/NETWORKS/8D.

Thomasset, C., Ritz, J.-F., Pouliquen, S., Manchuel, K., and Le-Roux-Mallouf, R. Geometry and tectonic history of the Northeastern Cévennes Fault System (Southeast Basin, France) : new insights from deep seismic reflection profiles. *BSGF - Earth Sciences Bulletin*, 195:17, 2024. doi: 10.1051/bsgf/2024016.

Thouvenot, F., Fréchet, J., Tapponnier, P., Thomas, J.-C., Le Brun, B., Ménard, G., Lacassin, R., Jenatton, L., Grasso, J.-R., Coutant, O., Paul, A., and Hatzfeld, D. TheML5.3 Épagny (French Alps) earthquake of 1996 July 15: a long-awaited event on the Vuache Fault. *Geophysical Journal International*, 135(3):876–892, Dec. 1998. doi: 10.1046/j.1365-246x.1998.00662.x.

Thouvenot, F., Jenatton, L., and Gratier, J. 200-m-deep earthquake swarm in Tricastin (lower Rhône Valley, France) accounts for noisy seismicity over past centuries. *Terra Nova*, 21(3):203–210, May 2009. doi: 10.1111/j.1365-3121.2009.00875.x.

Tinti, E., Fukuyama, E., Piatanesi, A., and Cocco, M. A Kinematic Source-Time Function Compatible with Earthquake Dynamics. *Bulletin of the Seismological Society of America*, 95(4): 1211–1223, Aug. 2005. doi: 10.1785/0120040177.

Traversa, P., Maufroy, E., Hollender, F., Perron, V., Bremaud, V., Shible, H., Drouet, S., Guéguen, P., Langlais, M., Wolyniec, D., Péquegnat, C., and Douste-Bacque, I. RESIF RAP and RLBP Dataset of Earthquake Ground Motion in Mainland France. *Seismological Research Letters*, 91(4):2409–2424, May 2020. doi: 10.1785/0220190367.

Tsai, Y.-B. and Aki, K. Precise focal depth determination from amplitude spectra of surface waves. *Journal of Geophysical Research*, 75(29):5729–5744, Oct. 1970. doi: 10.1029/jb075i029p05729.

Türker, E., Cotton, F., Pilz, M., and Weatherill, G. Analysis of the 2019 Mw 5.8 Silivri Earthquake Ground Motions: Evidence of Systematic Azimuthal Variations Associated with Directivity Effects. *Seismological Research Letters*, 93(2A):693–705, Jan. 2022. doi: 10.1785/0220210168.

University of Genoa. Regional Seismic Network of North Western Italy, 1967. doi: 10.7914/SN/GU.

Vallage, A., Bollinger, L., Champenois, J., Duverger, C., Trilla, A. G., Hernandez, B., Pichon, A. L., Listowski, C., Mazet-Roux, G., Menager, M., Pinel-Puysségur, B., and Vergoz, J. Multitechnology characterization of an unusual surface rupturing intraplate earthquake: the ML 5.4 2019 Le Teil event in France. *Geophysical Journal International*, 226(2):803–813, Apr. 2021. doi: 10.1093/gji/ggab136.

Wald, D. J. and Allen, T. I. Topographic Slope as a Proxy for Seismic Site Conditions and Amplification. *Bulletin of the Seismological Society of America*, 97(5):1379–1395, Oct. 2007. doi: 10.1785/0120060267.

Wang, X., Fu, C., Gu, W., Xie, C., Yao, Z., Sheng, S., Tian, X., and Deng, Z. The Magnitude 4.5 Earthquake in the Karst Area of Guizhou on 21 August 2021: An Extremely Shallow Earthquake with a Closing-Crack Source. *Seismological Research Letters*, Mar. 2023. doi: 10.1785/0220220360.

Wathelet, M., Guillier, B., Roux, P., Cornou, C., and Ohrnberger, M. Rayleigh wave three-component beamforming: signed ellipticity assessment from high-resolution frequency-wavenumber processing of ambient vibration arrays. *Geophysical Journal International*, 215(1):507–523, July 2018. doi: 10.1093/gji/ggy286.

Weatherill, G., Kotha, S. R., and Cotton, F. A regionally-adaptable "scaled backbone" ground motion logic tree for shallow seismicity in Europe: application to the 2020 European seismic hazard model. *Bulletin of Earthquake Engineering*, 18(11): 5087–5117, July 2020. doi: 10.1007/s10518-020-00899-9.

Weatherill, G. A. and Danciu, L. Regional variation of spectral parameters for seismic design from broadband probabilistic seismic hazard analysis. *Earthquake Engineering & Structural Dynamics*, 47(12):2447–2467, July 2018. doi: 10.1002/eqe.3092.

Zhao, L., Paul, A., Solarino, S., and RESIF. Seismic network XT: CIFALPS-2 temporary experiment (China-Italy-France Alps seismic transect #2, 2018. doi: 10.15778/RESIF.XT2018.